RESEARCH ARTICLE

Magnetohydrodynamic Flow and Heat Transfer of Boger Tri-Hybrid Nanofluid over a Porous Disk with Cattaneo-Christov Heat Flux Theory Using Artificial Neural Network Framework

Sohail Rehman[1,*]

[1] Department of Physical and Numerical Sciences, Qurtuba University of Science and Information Technology, Peshawar, KP 25000, Pakistan

Abstract

This study investigates the magnetohydrodynamic (MHD) flow of Boger tri-hybrid nanofluid (tri-HNF) through a stretching disk. A novel machine learning technique, specifically the Levenberg–Marquardt (LM) scheme under a backpropagated artificial neural network (ANN), is used to predict the flow dynamics with heat and mass transfer. The Cattaneo-Christov mass and heat fluxes model, permeable media, and viscous dissipation are considered. The well-known Brinkman-Hamilton and Crosser model is used to describe thermal conductivity and viscosity models. The computational solution to the current problem has been obtained using the Bvp4c approach, which is based on finite differences. In order to examine the numerical solutions and anticipated outcomes, LM-BNN uses a numerical dataset that is split into three categories: 15% for testing, 70% for training, and 15% for validation. Regression analysis, surface stresses, error histogram, correlation index, heat and mass transfer, and mean squared error-based fitness curves, which range from 10^{-10} to 10^{-8} are used to validate the consistency and efficacy of LM-BNN. The findings suggest that the velocity profile declines with the magnetic and relaxation time ratio parameter. The temperature and concentration decrease with thermal and solutal relaxation parameters. The heat and mass transfer rates are significant for solvent viscosity and nanomaterials load.

Keywords: boger fluid, modified fourier's and fick's laws, MHD, permeable medium, artificial intelligence, soft computing.

1 Introduction

The Boger fluid (BF) is classified as a viscoelastic liquids with constant viscosity, having special characteristics of rheology [1, 2]. Compared to other viscoelastic fluids, they sustain a consistent viscosity even when squeezed because of their extremely diluted

Submitted: 23 August 2025
Accepted: 29 September 2025
Published: 26 October 2025

Vol. 1, **No.** 3, 2025.
10.62762/JAM.2025.640044

***Corresponding author:**
Sohail Rehman
sohail08ktk@gmail.com

Citation
Rehman, S. (2025). Magnetohydrodynamic Flow and Heat Transfer of Boger Tri-Hybrid Nanofluid over a Porous Disk with Cattaneo-Christov Heat Flux Theory Using Artificial Neural Network Framework. *ICCK Journal of Applied Mathematics*, 1(3), 97–119.

composition, which inhibits shear-thinning behavior. These fluids are made by mixing a small quantity of polymer with a high-viscosity non-Newtonian fluid, like corn syrup and polyacrylamide. The shear-thinning effects and elastic character can be easily distinguished in experiments because to its composition. Through the comparison of Newtonian liquids with the same viscosity and BF, the researchers can determine elasticity effects, flow rates, which offers important information about non-Newtonian behavior. The unique rheological characteristics of BF make it valuable in a wide range of industries [3, 4]. The BF is used to understand the dynamics of complex fluids. The BF is utilized in biomedical research to simulate biological fluid viscosity, which aids in the development of medical equipment and drug delivery systems. They are also utilized in the manufacturing of consumer items, including as food and beauty products, where precise control over viscosity is crucial. The BF are used to improve the efficiency of the drilling process in the oil and gas industry. Additionally, they are used in the development of damping systems that ensure stability and security in engineering structures. In recent study, James et al. [5], examined the pressure droplet in a converging conduit. They found that the non-Newtonian pressure dips were up to multiple times greater, despite the apparent lack of elasticity. A computational and experimental study was conducted by López-Aguilar [6] to examined the pressure drop of BF in a sharp contraction. They utilized finite element method to solve the governing equations. The Taylor vortex flows of BF between an oscillating cylinder was investigated by Choujaa et al. [7]. They arrived at the conclusion that the essential vortex flow conditions at the commencement of instability are clarified by the influence of both the polymer elasticity and the polymer-solvent viscosity ratio. The finite element investigation of monolayer thermal conductivity in Boger nanofluid (BNF) flow with motile microorganisms under variable conditions was scrutinized by Raza et al. [8]. They concluded that the velocity of NF improve with solvent fraction, but reduces as the relaxation time ratio. Few recent theoretic and experimental studies on BNF and BF are captured in the studies [9–11].

Fluid flow over a stretching disk refers to a revolving or radially stretching surface that induces fluid motion, commonly used for the analysis of boundary layer flows (BLF), energy transfer, and mass transport [12]. This type of flow is particularly significant in industrial applications such as polymer processing, rotating machinery, and aerodynamic systems, where the stretching motion effects fluid dynamics by modifying velocity and heat profiles. The problem is commonly modeled using the von Kármán similarity approach [13], which simplifies the Navier-Stokes equations into ordinary differential equations, permitting investigation of flow behavior under varying stretching rates, rotation speeds, and heat conditions. Research on stretching disks helps to optimize processes including coating, crystal formation, and centrifugal transporting by understanding how surface motion influences the surface drag, heat transfer, and fluid stability [14]. The study of NF over a stretching disks in incidence of gyrotactic microorganisms was examined by Chu et al. [15]. They found that velocity is higher against stretching parameter. The convective flow of Casson NF through a stretching rotating disk in the incidence of magnetic force and nonlinear thermal radiation was elaborated by [16]. Their findings demonstrate that an increasing in the nanoparticle volume fraction triggers the velocity to decrease in the radial direction while increasing the temperature and velocity in the azimuthal direction. The computational analysis of mass and heat transfer in MHD NF flow over a revolving disk with fluid variable features was investigated by Sharma et al. [17]. It was concluded that the radial motion is much enhanced by disk spinning, whereas other parameters like Reynolds number, fluctuating viscosity, and magnetic field variable show a reduction. Rehman [18] examined the BLF flow with heat and mass transfer features over a permeable disk taking activation energy and Darcy-Forchheimer model. He concluded that, adding copper nanoparticles enhances the lubrication effects at the boundary and raises the skin friction. Additionally, a 3% load of copper nanomaterial results in significant improvements in heat and mass transfer.

There are numerous heat transfer mechanisms used in common industrial operations, such as space-based cooling structures, heat exchangers, and the distribution of moisture and temperature across groove fields [19]. A significant disadvantage of the classical Fourier heat flow rule [20] is that it does not satisfy the well-known causality principle, despite the fact that it is the favored model for energy transfer in many real-world scenarios. As a modified version of Fourier's law, the Cattaneo-Christov heat flux (CCHF) model accounts for a lag in heat propagation by incorporating a finite thermal relaxation period [21, 22]. This non-Fourier framework is especially

pertinent in biomedical settings, where the actual process of heat transfer in living tissues, implants, and small-sized devices is not adequately captured by the assumption of continuous heat conduction [23]. Through the consideration of non-instantaneous thermal responses, the model considerably improves the accuracy of thermal studies in applications like cryotherapy, laser-based therapies, and thermal surgical ablation. The thermal flux and temperature gradient are directly related, according to the traditional Fourier law of heat conduction. A parabolic heat equation can be derived mathematically from this relation, suggesting that thermal perturbations spread instantly across the medium [24]. In some recent studies, Saravanan et al. [25] examined the CCHF theory in a turbulence flow inside a heated mounted enclosure. They came to the conclusion that even after a slightly chaotic motion appears in tall enclosures, temperature relaxation strengthens periodic locking. In square enclosures, the CCHF inhibits the formation of bifurcations and postpones the commencement of turbulence; in tall enclosures, the reverse effect is observed. The role of CCHF on convection unsteadiness in a upright Brinkman permeable layer was examined by Jia et al. [26]. They concluded that, the vibrations induced in the neutral equilibrium curves vibrations rises as Cattaneo number increases. Shah et al. [27], provide non-similar solutions for two-phase hybrid NF flow with CCHF model.

Engineers are showing interest in using NF, which are made up of nanomaterials scattered throughout fundamental fluids, as a solution to renewable energy and heat administration issues. These innovative fluids are useful in a variety of applications, including renewable energy sources and electronics cooling, because they have improved heat transfer properties and enhanced thermal conductivity [28]. The effectiveness of NF is still being improved by research in a variety of applications, including electric vehicle batteries, industrial heat exchangers, air conditioners, radiators, and solar energy systems. Currently, researchers are focusing on improving nanoparticle stability and efficiency by optimizing their size, shape, and composition of material [29–31]. Prospective stability, adverse environmental impacts, and economic feasibility are among issues being addressed by advancements in NF research. NF are therefore poised to become a key technology in the pursuit of improved, sustainable, and cost-effective energy systems.

Tri-hybrid NF (THNF) are a revolutionary development in thermal fluids engineering that build on the accomplishments of hybrid NF. THNF incorporate three distinct kinds of nanoparticles into a base fluid, in contrast to hybrid NF, which combine two different types of nanoparticles, or standard NF, which use only one type of nanoparticle. While reducing the drawbacks of single and binary NF systems, this multi-component technique provides a very efficient way to improve thermal conductivity, heat transmission efficiency, and overall fluid stability [32, 33]. The intrinsic drawbacks of conventional NF provide the rationale for creating THNF. Although mono and hybrid NF have shown notable gains in heat transfer efficiency, they frequently face trade-offs between increased viscosity, improved thermal conductivity, and particle stability. Through the integration of three comparable nanoparticles, THNF have a synergistic effect that maximizes thermophysical performance in a variety of dimensions [34]. Compared to basic and hybrid NF, THNF has better heat transmission and thermal conduction properties. Because of this property, THNF shows great promise for enhancing energy efficiency and cooling in a variety of applications, including nuclear reactors and microfluidic equipment [35]. A number of variables affect THNF efficacy, such as the kinds, sizes, and forms of the nanoparticles and the proportions of the basic fluids and combination [36–39]. The integration of non-Newtonian rheology, MHD, and slip boundary conditions in THNF systems is still lacking, despite these advancements, particularly in the presence of stretching disk flow circumstances. This study fills that gap by examining the stretching disk flow of MHD Boger THNF driven by CCHF. It offers a unique viewpoint that combines sophisticated fluid behavior with useful heat transfer concerns.

Neural networks (NNs) are extensively utilized in a number of domains, such as economic research, enterprise strategy, commerce, handling finances, and manufacturing maintenance. Corporate applications including assessment of risks, recognizing fraud, marketing study, and forecasting also heavily rely on them. Backpropagation is one of the learning techniques most frequently utilized in multilayer NNs. This approach has been used recently to investigate heat transfer and fluid flow regimes. In order to investigate the performance of NNs in modeling a simultaneous grinding process, Mukherjee and Routroy [40] combined the gradient descent approach with Levenberg-Marquardt (LM)-algorithms and

Quasi-Newton. Similar to this, Aljohani et al. [41] used NNs to analyze intelligent computing by numerically analyzing a model with non-Newtonian wire covering. There are innumerable interlinked nodes (neurons) in each of the layers that make up this network. NNs constructed using machine learning (ML) include the multilayer perceptron (MLP), which is used in voice recognition and intelligent searching, deep NNs (DNNs), convolutional neuronal networks (CNNs), and the backpropagation algorithm, which is used in financial forecasting. The activation function of these networks is logistic functions. To deal with nonlinearity in fluid flow issues, the LM algorithm can quickly resolve. This model rheological characteristics are highly effective for industrial processes such as material design, procedure optimization, quality control, and predictive modeling [42].

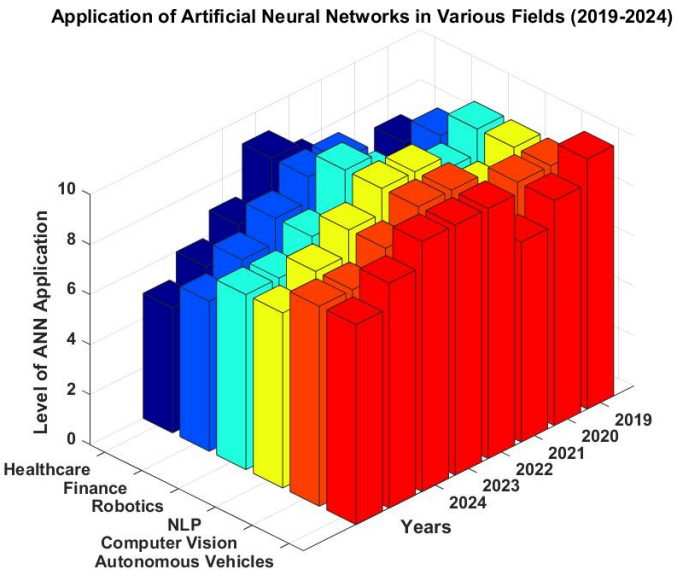

Figure 1. Application of ANN to real world problem.

Figure 1 illustrates the expanding applications of artificial neural networks (ANNs) from 2019 to 2024. The 3D bar chart shows a marked increase in adoption levels (on a scale of 0–10) across diverse sectors, including healthcare, finance, and autonomous vehicles. This trend underscores the versatility of ANNs in predictive modeling for complex real-world challenges, such as fluid dynamics and heat transfer. The uniqueness of this study is demonstrated by the way it presents a number of cutting-edge ideas that were not previously integrated into a single model. A Boger tri-HNF MHD flow over a porous disk has never been modeled before, despite the fact that Boger fluids and NF have been studied independently in the literature, as well as the Cattaneo-Christov heat flux and AI approaches. In a porous, MHD environment, the main research gap addressed is the absence of a thorough framework that concurrently takes into account the complicated rheology of Boger fluids, the improved thermal characteristics of a suspension of tri-nanoparticles, and non-Fourier heat and mass transfer. In order to close this gap and justify its innovation, the study uses a LM backpropagated ANN to produce a reliable and effective predictive solution. This contributes novel, credible data to the field of thermal engineering. This work uses ANN to investigate the heat and mass transport properties in MHD Boger tri-HNF flow across a porous medium in an effort to fill a gap in the existing literature. The LM-NN, which uses advanced features for efficient modeling and analysis, is used in this study. The study combines the Darcy-Forchheimer and CCHF models, using ANNs to model hybrid NF. As evidenced by the low mean square error (MSE) and absolute error (AE) values, the ANN makes predictions that are extremely accurate. The growing need for efficient heat transfer systems in sophisticated engineering applications subsequently spurred this investigation. The primary objectives include improving heat transfer efficiency, solving fluid dynamics computational challenges, and streamlining complex engineering systems. Applications requiring quick and efficient heat dissipation, such as cooling systems in the technological, transportation, and renewable energy sectors, are best suited for tri-HNF. By providing insights into the behavior of tri-HNF under complex boundary and magnetic settings, the research also aims to improve thermal systems and materials.

2 Constitutive equations

The constitutive law for stress and equations for mass balance, energy, mass concentration, and momentum transit control the flow of an incompressible viscoelastic fluid. Analysis of mass and heat transfer is carried out using relaxation of mass fluxes and heat fluxes, respectively, in the presence of viscous dissipation and mass diffusions. In non-dimensional form the constitutive equations are represented by [43, 44]:

$$\nabla \cdot \vec{V} = 0, \tag{1}$$

$$\rho\left(\vec{V} \cdot \nabla \vec{V}\right) = \nabla \cdot \sigma + F_{ext}, \tag{2}$$

$$(\rho c_p)\left(\vec{V} \cdot \nabla T\right) = -\nabla \cdot q_h + \sigma \cdot \nabla \vec{V}, \tag{3}$$

$$\left(\vec{V} \cdot \nabla C\right) = -\nabla \cdot q_m. \tag{4}$$

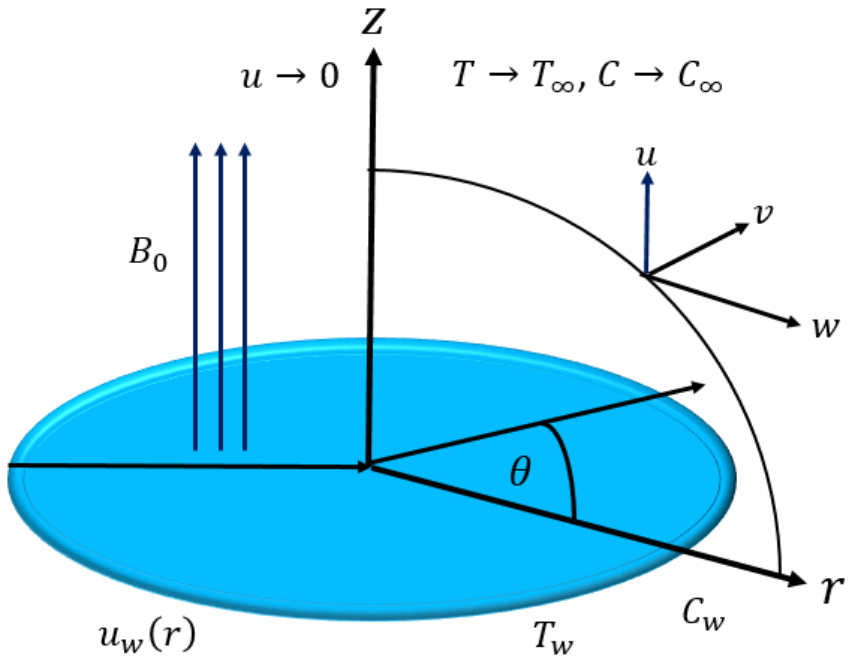

Figure 2. Problem illustration and coordinates system.

The BF model, a prominent constitutive model in rheology, is used to study the flow characteristics of viscoelastic materials including polymers and some complex fluids. The BF is widely used to describe materials that exhibit both viscous and elastic behavior for the study of features such as shear-thinning and viscoelasticity. The BF model demonstrated here obey the following constitutive equation [45, 46]:

$$\sigma = -pI + 2\mu_s D + \sigma_p. \tag{5}$$

where

$$\sigma_p = 2\mu_0 D, \quad \text{and} \quad \mu_0 = \mu_s + \mu_p. \tag{6}$$

here, $D = \frac{1}{2}\left(\nabla V + \nabla V^T\right)$ is the deformation rate, μ_s is solvent viscosity, μ_p is the polymeric viscosity, and p is the pressure term. In energy and concentration equations q_h and q_m are double diffusion heat and mass fluxes. The generalized Fourier's and Fick's law assuming incompressible flow $\nabla \cdot \vec{V} = 0$, and steady flow conditions takes the following form [47, 48]:

$$q_h + \lambda_1 \left(\vec{V} \cdot \nabla q_h - q_h \cdot \nabla \vec{V}\right) = -k_f \nabla T, \tag{7}$$

$$q_m + \lambda_2 \left(\vec{V} \cdot \nabla q_m - q_m \cdot \nabla \vec{V}\right) = -D_m \nabla C. \tag{8}$$

Equation (7) and (8) restore to classical Fourier's and Fick's law taking $\lambda_1 = \lambda_2 = 0$. Furthermore, F_{ext} is the external force in momentum conservation which is the sum of Lorentz force and Darcy law [49]. Mathematically,

$$F_{ext} = F_L + F_p. \tag{9}$$

where

$$F_L = \vec{J} \times \vec{B}, \quad \text{and} \quad F_p = \nabla p = -\frac{\mu \vec{V}}{K}. \tag{10}$$

where $\vec{J}$ is the current density, $\vec{B}$ is the magnetic field strength, and K is the medium permeability.

3 Governing problem

Consider the MHD Boger tri-HNF across a stretching disk dipped in a porous material. The cylindrical coordinate system (r, θ, z) is adopted for problem formulation as depicted in Figure 2. It is assumed that the flow of mixture fluid take place along circular disk located at $z = 0$. The circular disk stretches with stretching rate of br. The fluid is made up of three different kinds of nanoparticles: silver (Ag), Copper (Cu) and magnesium oxide (MgO). The derivatives along the tangential coordinate θ may be disregarded because of the axial symmetry. Let $T = T(r, z)$ and $C = C(r, z)$ are the temperature and concentration distribution and $\vec{V} = (u(r, z), 0, w(r, z))$ be the velocity vector. The generalized Fick's law, and Fourier's

law are deployed in energy and mass concentration equations. The well-known Brinkman-Hamilton and Crosser models are considered for effective viscosity and thermal conductivity.

The flow is laminar, incompressible, steady, and two-dimensional flow equations takes the following form [18, 50]:

$$\frac{\partial u}{\partial r}+\frac{u}{r}+\frac{\partial w}{\partial z}=0, \tag{11}$$

$$\left(u\frac{\partial u}{\partial r}+w\frac{\partial w}{\partial z}\right)=\frac{\mu_{thnf}}{\rho_{thnf}}\left(\left(\frac{1+\alpha_1}{1+\alpha_2}\right)\frac{\partial^2 u}{\partial z^2}\right) - \frac{\sigma_{thnf}B_0^2 u}{\rho_{thnf}}-\frac{\mu_{thnf}}{\rho_{thnf}}\frac{u}{K}, \tag{12}$$

$$\begin{aligned}&\left(u\frac{\partial T}{\partial r}+w\frac{\partial T}{\partial z}\right)\\&=\frac{k_{nf}}{(\rho c_p)_{thnf}}\frac{\partial^2 T}{\partial z^2}+\frac{\mu_{nf}}{(\rho c_p)_{thnf}}\left(\left(\frac{1+\alpha_1}{1+\alpha_2}\right)\left(\frac{\partial u}{\partial z}\right)^2\right)\\&-\lambda_1\left(u^2\frac{\partial^2 T}{\partial r^2}+w^2\frac{\partial^2 T}{\partial z^2}+2uw\frac{\partial^2 T}{\partial r\partial z}\right.\\&\left.+\left(u\frac{\partial u}{\partial r}+w\frac{\partial u}{\partial z}\right)\frac{\partial T}{\partial r}+\left(u\frac{\partial w}{\partial r}+w\frac{\partial w}{\partial z}\right)\frac{\partial T}{\partial z}\right),\end{aligned} \tag{13}$$

$$\begin{aligned}&\left(u\frac{\partial C}{\partial r}+w\frac{\partial C}{\partial z}\right)\\&=D_M\left(\frac{\partial^2 C}{\partial z^2}\right)-\lambda_2\left(u^2\frac{\partial^2 C}{\partial r^2}+w^2\frac{\partial^2 C}{\partial z^2}+2uw\frac{\partial^2 C}{\partial r\partial z}\right.\\&\left.+\left(u\frac{\partial u}{\partial r}+w\frac{\partial u}{\partial z}\right)\frac{\partial C}{\partial r}+\left(u\frac{\partial w}{\partial r}+w\frac{\partial w}{\partial z}\right)\frac{\partial C}{\partial z}\right).\end{aligned} \tag{14}$$

The boundary conditions for the problem are [51, 52]:

$$u\to u_w(r)=br+\nu_{thnf}S_1\left(\frac{1+\alpha_1}{1+\alpha_2}\right)\left(\frac{\partial u}{\partial z}\right),$$

$$w=0,\quad T=T_w,\quad C=C_w,\quad \text{as } z=0, \tag{15}$$

$$u\to cr,\quad T\to T_\infty,\quad C\to C_\infty,\quad \text{as } z\to\infty. \tag{16}$$

where α_1 and α_2 are the BF parameters, the symbol K refer to the porosity of the medium, S_1 is the slip parameter, λ_1 and λ_2 are the thermal and solutal relaxation parameters, respectively.

In order to transform the governing PDE into a system of ODEs, the following similarity transformation are deployed [18, 53]:

$$\begin{aligned}&u=brf'(\eta),\quad w=-2\sqrt{b\nu_f}f(\eta),\quad \Theta(\eta)=\frac{T-T_\infty}{T_m-T_0},\\&\chi(\eta)=\frac{C-C_\infty}{C_m-C_0},\quad \eta=z\left(\frac{a}{\nu_f}\right)^{\frac{1}{2}}.\end{aligned} \tag{17}$$

The transport equations are reduced into a system of ODEs:

$$A_1\left(\frac{1+\alpha_1}{1+\alpha_2}\right)f'''-A_2\left(f'^2-2f''f\right)-A_2\left(P_o f'\right)-A_3M_a f'=0, \tag{18}$$

$$\begin{aligned}&A_5\Theta''-A_4\,\mathrm{Pr}\left(f\Theta'-2f'\Theta\right)+A_1A_4\,\mathrm{Pr}\,Ec\left(\frac{1+\alpha_1}{1+\alpha_2}\right)f''^2\\&-\mathrm{Pr}\,\varepsilon_T\left(f^2\Theta'-ff'\Theta'-ff''\Theta+f'^2\Theta''\right)=0,\end{aligned} \tag{19}$$

$$\begin{aligned}&\Psi''+Sc\left(f\Psi'-2f'\Psi\right)\\&-Sc\varepsilon_c\left(f^2\Psi'-ff'\Psi'-ff''\Psi+f'^2\Psi''\right)=0,\end{aligned} \tag{20}$$

with

$$\begin{aligned}&f'(0)+L_1\frac{\nu_{thnf}}{\nu_f}\left(\left(\frac{1+\alpha_1}{1+\alpha_2}\right)f'^2(0)\right)\\&f(0)=0,\quad \Theta(0)=0,\quad \Psi(0)=0.\end{aligned} \tag{21}$$

$$f'(\infty)=B,\quad \Theta(\infty)=0,\quad \Psi(\infty)=0. \tag{22}$$

The physical quantities such as skin friction C_f, Nusselt Nu and Sherwood number Sh are modeled using following equations:

$$C_{fr}=\frac{\tau_{wr}}{\rho_{thnf}u_w^2},\quad \text{where}\quad \tau_{wr}=2\ \mu_{thnf}\left(\left(\frac{1+\alpha_1}{1+\alpha_2}\right)\frac{\partial u}{\partial z}\right)\Big|_{z=0}, \tag{23}$$

$$Nu_r=\frac{xq_w}{k_{thnf}\left(T_w-T_\infty\right)},\quad \text{where}\quad q_w=-\ k_{thnf}\left(\frac{\partial T}{\partial z}\right)\Big|_{z=0}, \tag{24}$$

$$Sh_r = \frac{xq_m}{D_M\left(C_w - C_\infty\right)}, \quad \text{where} \quad q_m = -\ D_M\left(\frac{\partial C}{\partial z}\right)\Big|_{z=0}. \tag{25}$$

In dimensionless form

$$\frac{1}{2}\sqrt{Re_r}C_{fr} = A_2\left(\left(\frac{1+\alpha_1}{1+\alpha_2}\right)f'^2(0)\right), \tag{26}$$

$$Nu_r = -\sqrt{Re_r}A_5\left(\Theta'(0)\right), \tag{27}$$

$$Sh_r = -\sqrt{Re_r}\chi'(0). \tag{28}$$

where

$$L_1 = S_1\sqrt{\frac{b}{\nu_f}}, \quad P_o = \frac{\nu_f}{Kb}, \quad M_a = \sqrt{\frac{\sigma_f B_0^2}{b\rho_f}}, \quad B = \frac{c}{b},$$
$$Pr = \frac{\mu_f\left(c_p\right)_f}{k_f}, \quad Ec = \frac{u_w^2}{\left(c_p\right)_f\left(T_w - T_\infty\right)}, \quad Sc = \frac{\nu_f}{D_M},$$
$$\varepsilon_T = b\lambda_1, \quad \varepsilon_c = b\lambda_2, \quad Re_r = \frac{ru_w}{\nu_f}. \tag{29}$$

and

$$A_1 = \frac{\rho_{thnf}}{\rho_f}, \quad A_2 = \frac{\mu_{thnf}}{\mu_f}, \quad A_3 = \frac{\sigma_{thnf}}{\sigma_f},$$
$$A_4 = \frac{\left(\rho c_p\right)_{thnf}}{\left(\rho c_p\right)_f}, \quad A_5 = \frac{k_{thnf}}{k_f}. \tag{30}$$

The dynamics of NF expression are taken as suggested by [54, 55]. As shown in Table 1, the thermo-chem-physical features of water and the three nanomaterials are used to compute parameters such as effective density ρ_{thnf} and effective thermal conductivity k_{thnf}.

4 Methodology

4.1 Numerical scheme

The shooting technique is employed for computing the nonlinear coupled ordinary differential equations (18) and (19) with boundary conditions (21) using the Bvp4c solver, a built-in function computing tool in MATLAB. This is the point at which the higher-order system of equations becomes the first-order system. In Bvp4c, the initial guess is necessary for further computations. A guess is made at an initial mesh point, and the results are produced by increasing the step size until the desired level of precision is achieved. It is necessary to select the proper initial guess and boundary layer thickness based on the values of the parameters that were employed. In this problem, tolerance is taken into account 10^{-6}. The solution is validated with previous results in limiting scenario. The problem validation is provided in Table 2.

4.2 Implementation of Artificial neural network

The LM backpropagated ANN is a computational model that learns to identify tendencies and solve challenging tasks. It is modeled after the biological neural networks found in the human brain. Validation, testing, and training are the three main stages of the technique. Associated layers of artificial neurons (input, hidden, and output layers) process input data during training. Each layer has a weight that iteratively adjusts via the backpropagation to reduce the error between estimated and actual outputs using algorithmic techniques such as gradient descent. In order to avoid overfitting, the validation step adjusts hyperparameters (such as learning rate and number of layers), while the testing phase assesses the model performance using actual data. The ANN mimicked after the intricate network of neurons in the human brain, which has attracted a lot of interest lately. By mimicking evolutionary processes found in neural networks, they show similar efficacy to the human brain in terms of categorization, learning, classification, optimizing, prediction, and generalization [62, 63]. Different neural connection training and rule arrangements result in a wide range of network configurations. Dense connections between neurons usually give rise to layers. The data input, hidden, and output phases are typically included in an ANN design. After receiving external data, these tiers process it before sending it via the ANN. Data first goes through hidden layer neurons without going through the input layer. Weights, connecting lines, and neuron interconnections can all be changed to make translation easier. The system keeps track of input values and the weights assigned to them in an ANN training database. The best number of layered and hidden neurons is a crucial consideration in the construction of ANN. The frequency and quality of interneuron interconnections are represented by weights, where the ANN stores the information it acquired. The way these connections are structured allows for the classification of many types of neural network designs, including feed-forward neural networks (FFNN) and feed-backward neural networks (FBNN). The LM-BNN is used to assess the performance of the suggested Boger tri-HNF model.

Table 1. The thermo-chem-physical features of Water, and three nanomaterials [56–58].

Thermo-chem-physical features	ρ : $[\text{kg.m}^{-3}]$	$\sigma\ [\Omega.\text{m}^{-1}]$	$k\ [(\text{W.m}^{-1}.\text{K}^{-1})]$	$c_p\ [(\text{J.kg}^{-1}.\text{K}^{-1})]$
Water (H_2O)	997.01	5.5×10^{-6}	0.636	2415
Silver Ag	10,500	8.1×10^{6}	429	235
Copper Cu	8933	59.6×10^{6}	400	385
Magnesium oxide (MgO)	3560	1×10^{-8}	45	700

Table 2. Validation of the problem for skin friction $\frac{1}{2}\sqrt{Re_r}C_{fx}$ taking different values of M_a.

M_a	B	Khashi'ie et al. [59]	Rafique et al. [60]	Azhar et al. [61]	Present results
1.0	0.0	1.64532	1.64532	1.64532	1.64534
-	0.2	1.38320	1.38320	1.38320	1.38322
-	0.5	0.92353	0.92353	0.92353	0.92356
0.0	-	0.78032	0.78032	0.78032	0.78035
5.0	-	1.35766	1.35766	1.35766	1.35769
10.0	-	1.75767	1.75767	1.75767	1.75769

The most common type of ANN are feed-forward neural networks, which are usually trained using the backpropagation controlled learning algorithm. Backpropagation is used for updating the network's weights by comparing them to the gradient of a loss function. For a given input dataset, this loss function calculates the difference between the actual and expected outputs. A neural network with two outputs and ten hidden layers is created for the suggested BF model. Regression estimation purposes, error histogram analysis, and mean squared error value analysis using the tool command are used to validate the performance of its LM-ANN. The velocity, temperature, concentration, skin friction, Nusselt and Sherwood number results for input values ranging from 0 to $h = 1.6$, show substantial dispersion for planned LM-ANN execution. The numerical data set is divided into three parts: 15% for training, 70% for validation, and 15% for testing [64]. Figure 3, provide multilayer ANN model detail. In this model, there is one input, 10 hidden, and 7 output hidden neuron layers.

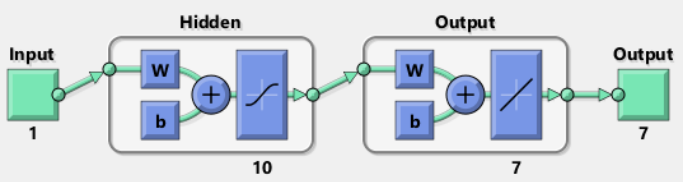

Figure 3. Neuron structure of ANN.

The most popular and well-respected training technique among researchers is frequently the LM algorithm. The resulting layer of ANN model uses the purelin function as its activation function, and the Tan-Sigmoid function [63] for the transfer function in the hidden layer.

$$f(\overline{x}) = \frac{1}{1+e^{-(\overline{x})}}, \quad purelin(\overline{x}) = \overline{x}. \tag{31}$$

The forecasting accuracy and operational efficiency of the ANN model must be evaluated after it has been designed. The $R-$squared error and MSE are calculated to assess the model efficacy. Here is the detail of MSE and R:

$$\text{MSE} = \frac{1}{n}\left(\sum_{j=1}^{n}\left(\mathbb{X}_{actual(j)} - \mathbb{X}_{predicted(j)}\right)^2\right), \tag{32}$$

$$R = \sqrt{1 - \frac{\sum_{j=1}^{n}\left(\mathbb{X}_{actual(j)} - \mathbb{X}_{predicted(j)}\right)^2}{\sum_{j=1}^{n}\mathbb{X}_{actual(j)}}}. \tag{33}$$

The relative error of ANN is further estimated by % error,

$$\%Error = \frac{\left(\mathbb{X}_{actual(j)} - \mathbb{X}_{predicted(j)}\right)}{\mathbb{X}_{actual(j)}} \times 100. \tag{34}$$

where $\mathbb{X}_{actual(j)}$ and $\mathbb{X}_{predicted(j)}$ are the actual and predicted values of ANN.

5 Results and discussion

The aim of this section is to elaborate the performance of flow, heat and mas transfer rate performance

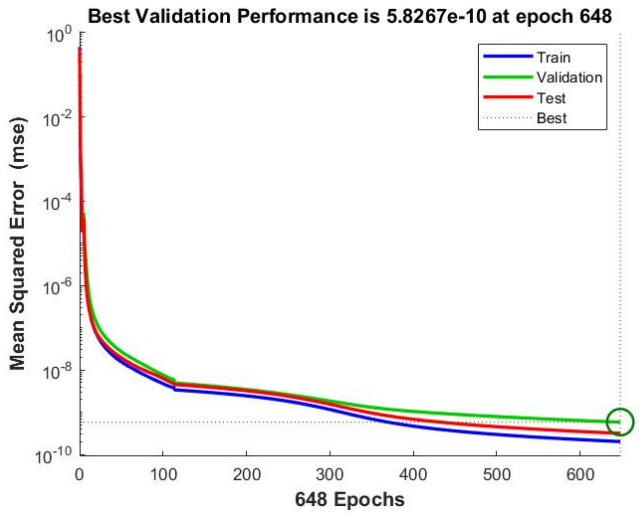

(a)C3S1

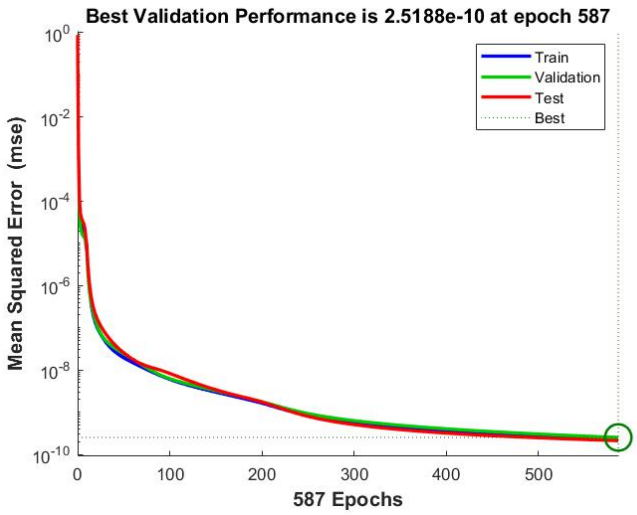

(b)C3S2

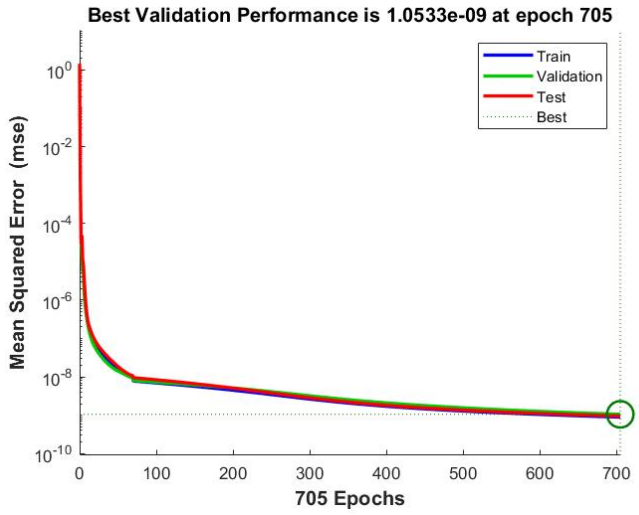

(c)C3S3

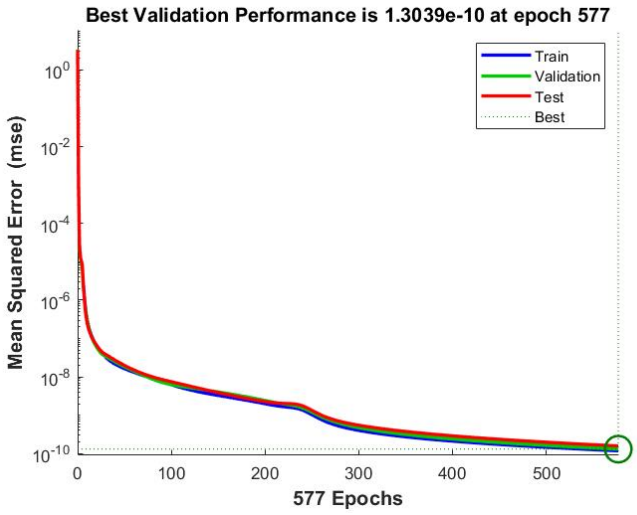

(d)C3S4

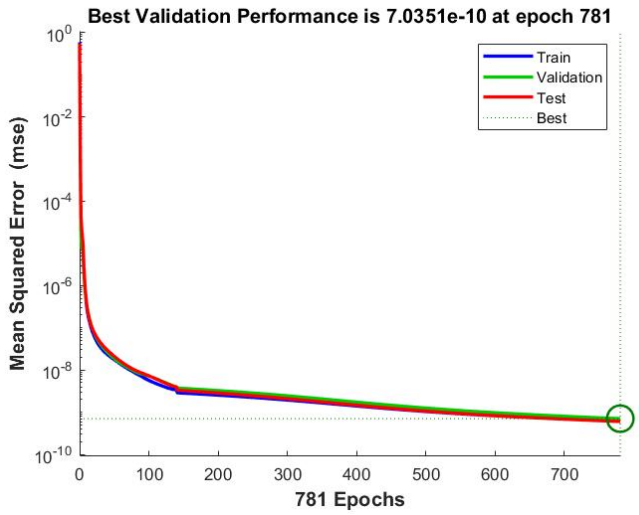

(e)C3S5

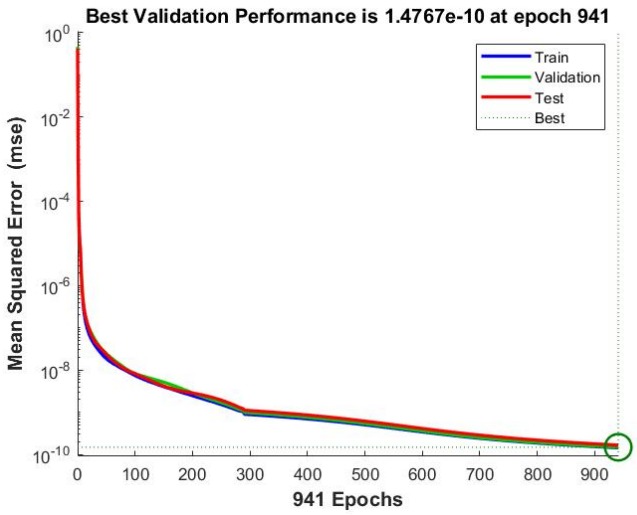

(f)C3S6

Figure 4. Performance of all scenario.

of Boger tri-HNF. The application and evaluation of LM back-propagating ANN for case 3 of the experiment (scenarios 1 through 6) are covered in depth. ANN has a hidden pattern with modules

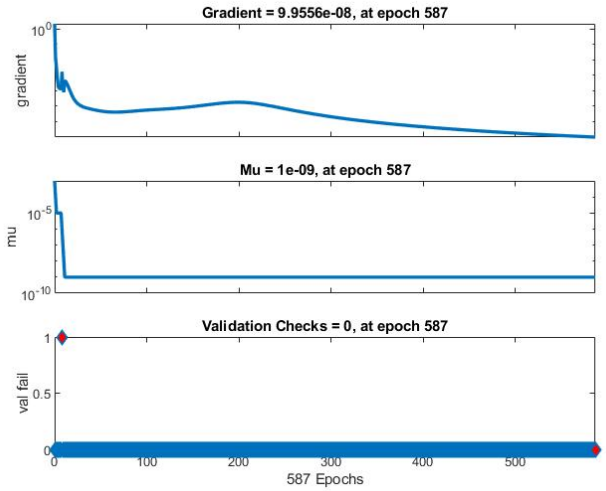

(a)C3S1

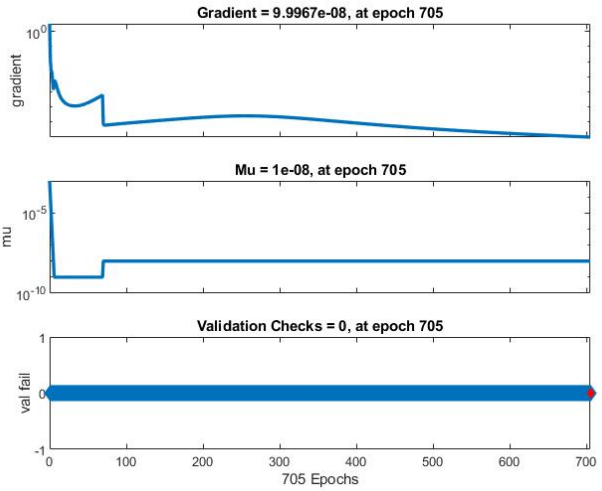

(b)C3S2

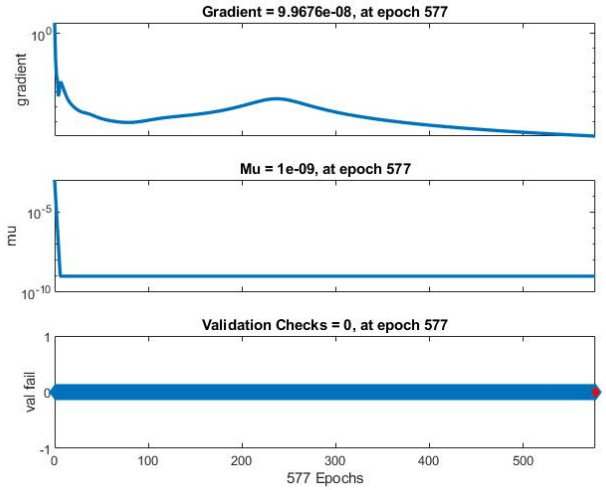

(c)C3S3

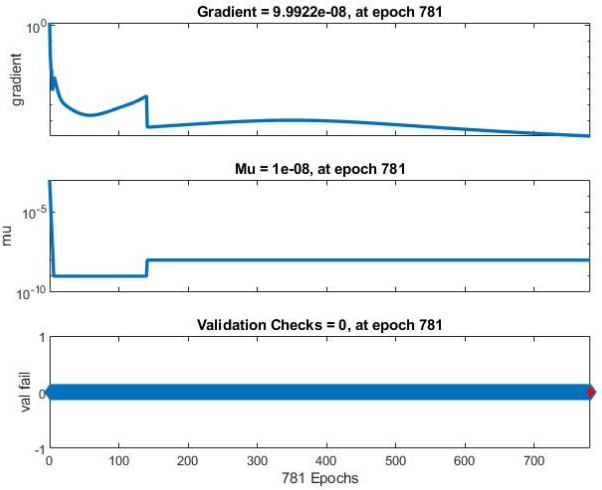

(d)C3S4

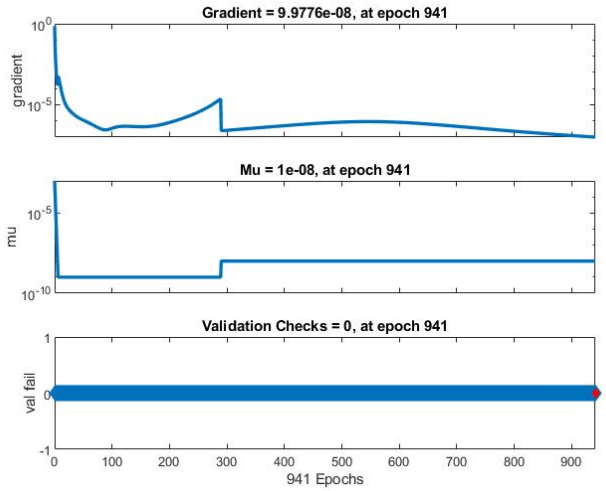

(e)C3S5

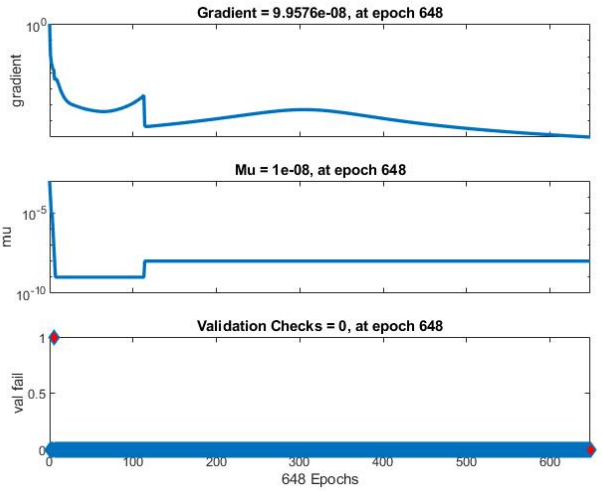

(f)C3S6

Figure 5. Transition State plots for all scenario.

that convert input to output in along with restricting the input layer and output layers. The Tri-HNF concentration, temperature, velocity, wall stresses, Nusselt, and Sherwood are examined. To illustrate

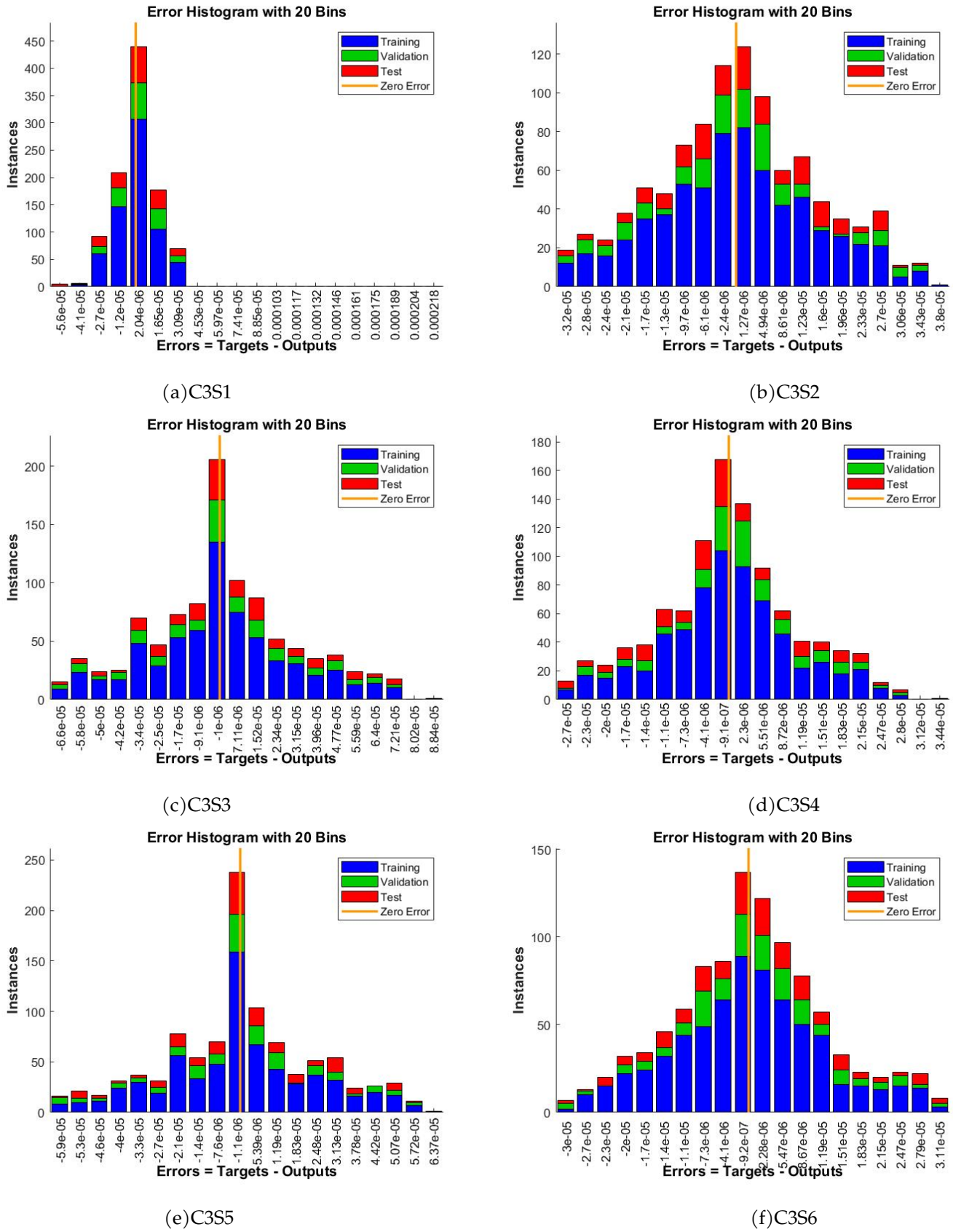

(a)C3S1 (b)C3S2

(c)C3S3 (d)C3S4

(e)C3S5 (f)C3S6

Figure 6. Error histograms for all scenario.

these charts, the ranges for those profiles between the highest and lowest points have been generated, and all of the values have been fixed. We have collected 100 metrics for these profiles. The effectiveness

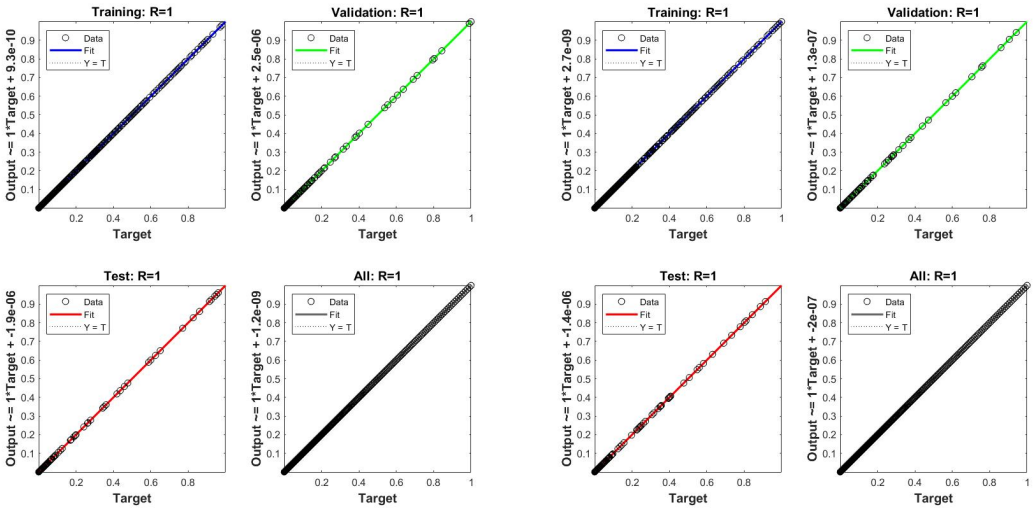

(a)C3S1

(b)C3S2

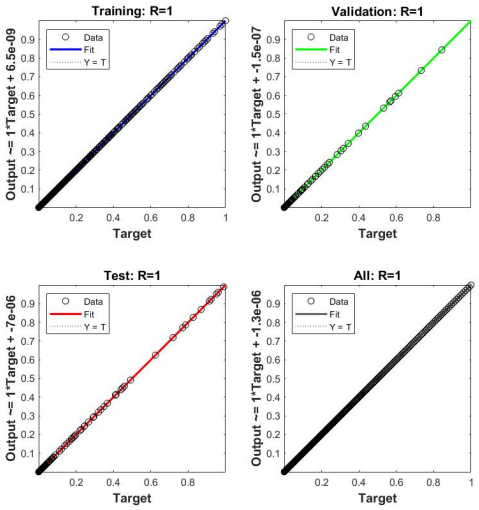

(c)C3S3

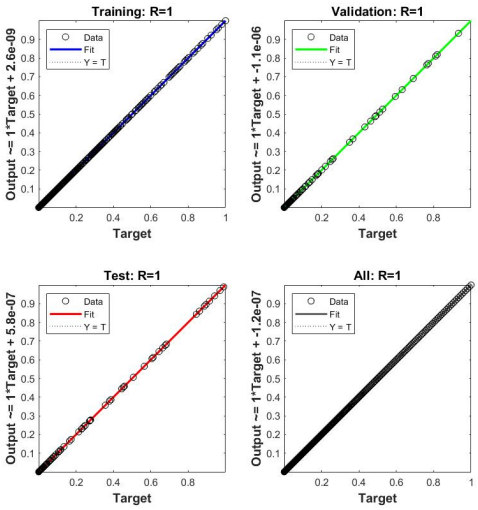

(d)C3S4

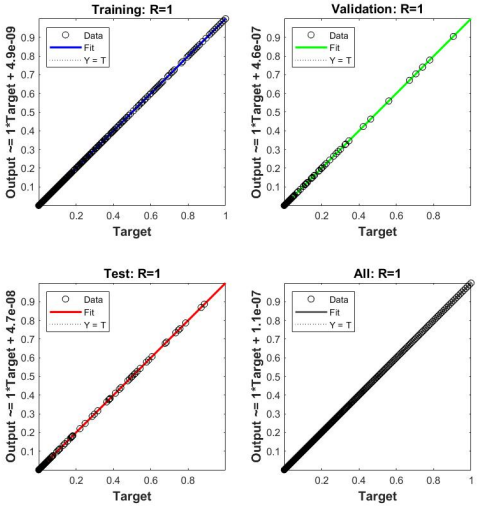

(e)C3S5

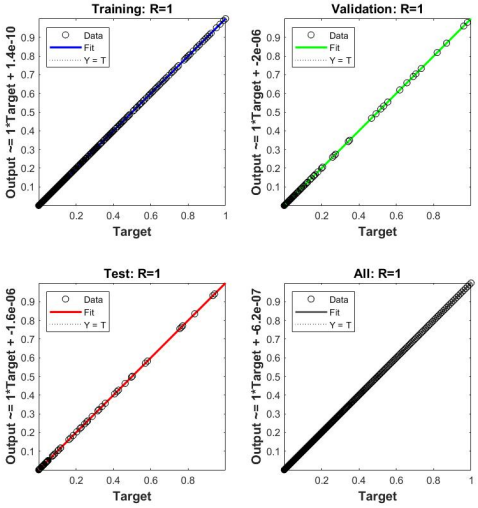

(f)C3S6

Figure 7. Regression plots for all scenario.

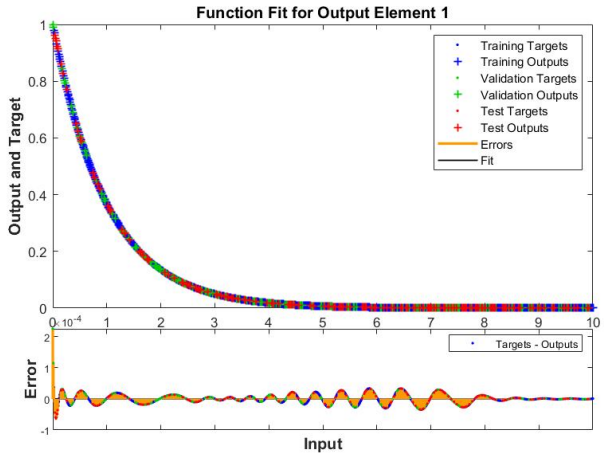

(a)C3S1

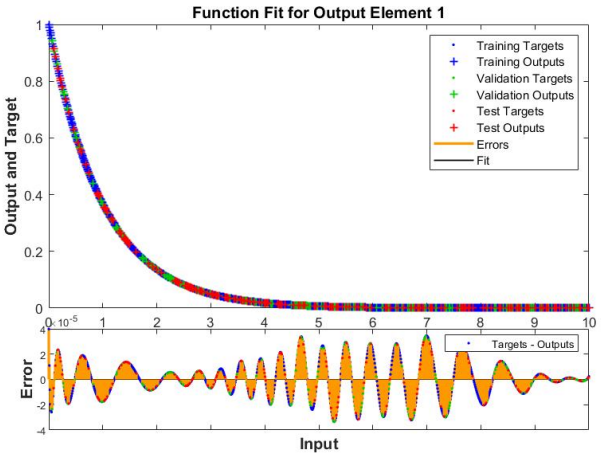

(b)C3S2

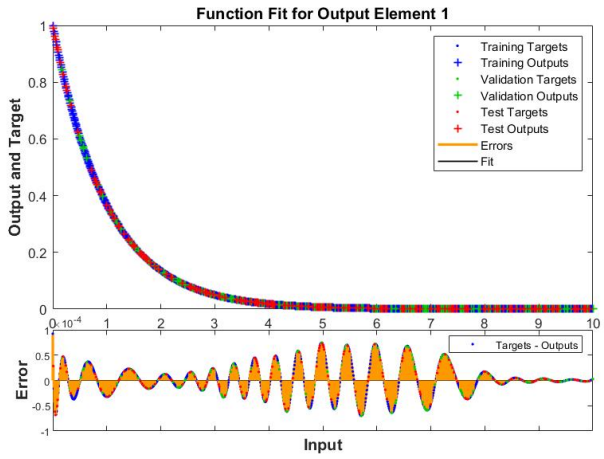

(c)C3S3

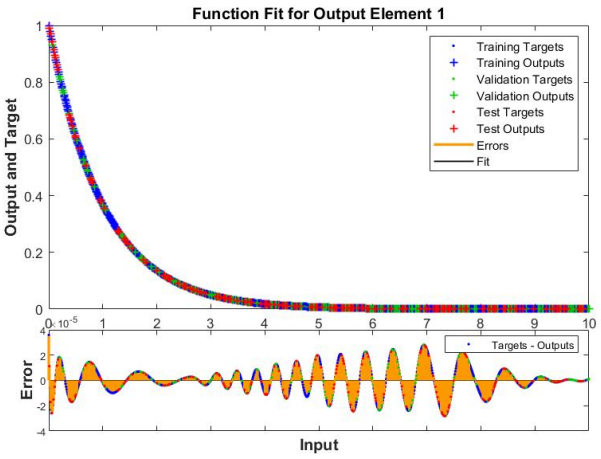

(d)C3S4

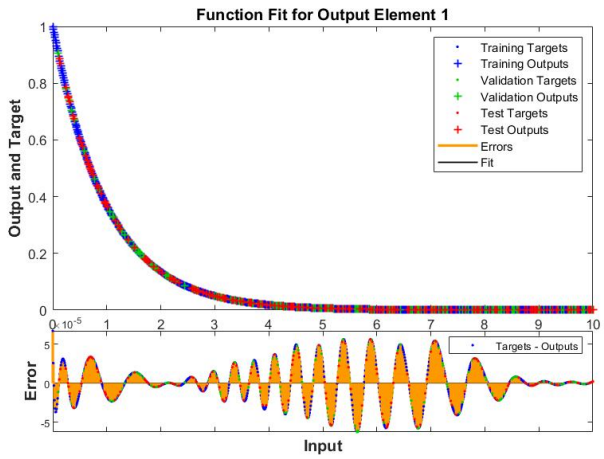

(e)C3S5

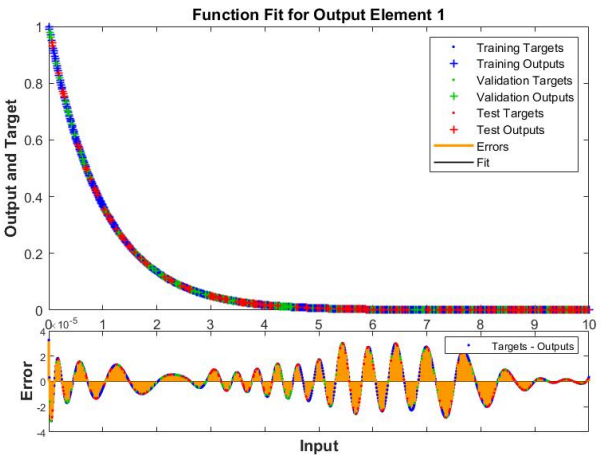

(f)C3S6

Figure 8. Fit plots for all scenrio.

of the ANN model is assessed using a variety of metrics, including the effectiveness curves for velocity profiles, phase changes, regression estimation, and error histograms. The estimated solution on the MSE source is constructed using the training data, the LM is constructed using the verification data, and the real input performance is verified using the test data. All of the parameters and cases for each scenario are shown

in Table 3. The MSE, time, number of epochs, and other convergence conditions are all listed in Table 4. The border stresses, Nusselt and Sherwood number details, and their inaccuracy are detailed in Tables 5, 6, and 7.

Table 3. Detail of governing parameters, scenario and cases.

Profiles	Cases	Parameters					
		α_1	α_2	ε_T	ε_c	M_a	P_0
Flow profile (S1)	1	0.0	0.0	0.0	0.0	0.0	0.0
	2	0.5	0.5	0.5	0.5	0.5	0.5
	3	1.0	1.0	1.0	1.0	1.0	1.0
Thermal profile (S2)	1	0.0	0.0	0.0	0.0	0.0	0.0
	2	0.5	0.5	0.5	0.5	0.5	0.5
	3	1.0	1.0	1.0	1.0	1.0	1.0
Concentration profile (S3)	1	0.0	0.0	0.0	0.0	0.0	0.0
	2	0.5	0.5	0.5	0.5	0.5	0.5
	3	1.0	1.0	1.0	1.0	1.0	1.0
Skin friction (S4)	1	0.0	0.0	0.0	0.0	0.0	0.0
	2	0.5	0.5	0.5	0.5	0.5	0.5
	3	1.0	1.0	1.0	1.0	1.0	1.0
Nusselt number (S5)	1	0.0	0.0	0.0	0.0	0.0	0.0
	2	0.5	0.5	0.5	0.5	0.5	0.5
	3	1.0	1.0	1.0	1.0	1.0	1.0
Sherwood number (S6)	1	0.0	0.0	0.0	0.0	0.0	0.0
	2	0.5	0.5	0.5	0.5	0.5	0.5
	3	1.0	1.0	1.0	1.0	1.0	1.0

The impact of layer size and epoch count on model efficiency is the main focus of this in-depth sensitivity investigation of the ANN configuration. Essential metrics like the correlation coefficient R, training time, number of epochs, and MSE are considered in the analysis. According to Figure 4(a-f), the results highlight the best ANN structure for striking a balance between accuracy and computing efficiency. The analysis highlights the model enhanced learning capability by showing that adding more layers dramatically lowers the MSE. A near-perfect match between the anticipated and actual values is indicated by the $R-$value, which is initially low for 2-layer networks but rapidly approaches 1.0 as the number of layers increases. The MSE epochs scores, which display the network performance at different intervals, are significant. The recorded MSE for all scenario S1, S2, S3, S4, S5 and S6 are 5.82×10^{-10} at 648 epochs, 2.51×10^{-10} at 587 epochs, 1.05×10^{-9} at 705 epochs, 1.30×10^{-10} at 577 epochs, 7.03×10^{-10} at 781 epochs and 1.47×10^{-10} at 941 epochs. Better performance is indicated by lower MSE. The learning accuracy of the network is indicated by these plots. The complexity and non-linearity of the simulated situations are highlighted by the range in epochs required to achieve these MSE, showing how different situations require different levels of training for optimal outcomes. Figure 5(a–f) shows the convergence performance, coherence, and predictability of case 3 simulation maintenance inside the architecture. The parameter Mu, which represents the gradients and step size, is an important consideration in this case. For all S1, S2, S3, S4, S5 and S6, the Mu value is set to 1×10^{-9}, 1×10^{-8}, 1×10^{-9}, 1×10^{-8}, 1×10^{-8} and 1×10^{-8}, respectively. The equivalent gradient values for each scenario are 9.95×10^{-8}, 9.99×10^{-8}, 9.96×10^{-8}, 9.99×10^{-8}, 9.95×10^{-8} and 9.97×10^{-8}. These figures show how the gradient responds to the Mu parameter, highlighting the network adaptive learning process. A notable pattern of decreasing Mu and gradient values over time is depicted in the graph, suggesting stability and convergence as well as the necessity for less network reconfiguration as it develops. This decrease demonstrates that the changes become less frequent and smaller as the network approaches peak performance. Additionally, it is associated with increased testing and training efficiency. Figure 6(a-f), which incorporates error histograms and fitness curves, provides a comprehensive behavioral assessment of errors. The error bar is a very helpful tool that illustrates the distribution of errors throughout the training process. As can be seen from the case 3 histogram, most errors are positive throughout scenarios (a-f), with the erroneous box of references mainly located above the zero axes. The network training methods can be improved and adjusted further in light of this tendency toward positive mistakes. In addition to the histogram, the fitness curves show how the network fitness has evolved over time. These results demonstrate the network capacity for error minimization and adaptation over training periods. These graphs indicate a tendency toward reducing errors, indicating the network's learning precision and effectiveness. In Figure 7(a-f), the linear regression investigation for case 3 scenarios (a-f) is reviewed. Understanding the relationship between input factors and the network's output forecasts is done using regression analysis. A greater correlation degree indicates better performance. The study demonstrates the degree of agreement between the expected and actual outcomes. The scatter plot in this image most likely has all of the points perfectly arranged along a line that signifies complete forecasting accuracy. The model functionality and possible areas for improvement are shown by any divergence from this line. It has been noted that

Table 4. The output of ANN for all scenario (S) and cases (C).

S	C	MSE Training	MSE Validation	MSE Testing	Performance	Gradient	Mu	Epoch	Time
	1	$3.5445E^{-9}$	$4.9335E^{-9}$	$3.6785E^{-9}$	$3.73E^{-9}$	$7.34E^{-9}$	$1.0E^{-9}$	456	1s
S1	2	$2.8899E^{-9}$	$3.8901E^{-9}$	$4.7890E^{-9}$	$3.89E^{-9}$	$8.45E^{-9}$	$1.0E^{-9}$	589	2s
	3	$3.5323E^{-9}$	$2.8932E^{-9}$	$3.5674E^{-9}$	$2.09E^{-9}$	$9.55E^{-9}$	$1.0E^{-9}$	648	2s
	1	$3.9078E^{-9}$	$4.8790E^{-9}$	$3.0982E^{-9}$	$3.92E^{-9}$	$7.56E^{-9}$	$1.0E^{-9}$	505	1s
S2	2	$3.7867E^{-9}$	$5.7889E^{-9}$	$2.8990E^{-9}$	$4.05E^{-9}$	$8.89E^{-9}$	$1.0E^{-9}$	563	1s
	3	$4.1235E^{-9}$	$5.9093E^{-9}$	$5.3454E^{-9}$	$4.23E^{-9}$	$9.99E^{-9}$	$1.0E^{-9}$	587	2s
	1	$3.2267E^{-9}$	$4.4455E^{-9}$	$3.5673E^{-9}$	$3.50E^{-9}$	$7.98E^{-9}$	$1.0E^{-9}$	305	1s
S3	2	$3.6789E^{-9}$	$4.5590E^{-9}$	$4.6787E^{-9}$	$3.45E^{-9}$	$8.09E^{-9}$	$1.0E^{-9}$	412	1s
	3	$4.8978E^{-9}$	$5.0233E^{-9}$	$4.8776E^{-9}$	$4.45E^{-9}$	$9.96E^{-9}$	$1.0E^{-9}$	705	2s
	1	$4.1234E^{-9}$	$4.4839E^{-9}$	$3.7334E^{-9}$	$3.78E^{-9}$	$8.12E^{-9}$	$1.0E^{-9}$	422	1s
S4	2	$4.3421E^{-9}$	$5.1234E^{-9}$	$4.7879E^{-9}$	$4.40E^{-9}$	$8.01E^{-9}$	$1.0E^{-9}$	508	2s
	3	$5.0191E^{-9}$	$5.9233E^{-9}$	$5.0916E^{-9}$	$5.10E^{-9}$	$9.99E^{-9}$	$1.0E^{-9}$	577	2s
	1	$4.1234E^{-9}$	$4.4839E^{-9}$	$3.7334E^{-9}$	$3.78E^{-9}$	$8.34E^{-9}$	$1.0E^{-9}$	487	2s
S5	2	$3.3421E^{-9}$	$4.1234E^{-9}$	$4.7879E^{-9}$	$3.34E^{-9}$	$9.02E^{-9}$	$1.0E^{-9}$	534	2s
	3	$5.0191E^{-9}$	$5.9233E^{-9}$	$5.0916E^{-9}$	$5.10E^{-9}$	$9.99E^{-9}$	$1.0E^{-9}$	781	2s
	1	$3.3457E^{-9}$	$3.8399E^{-9}$	$3.3394E^{-9}$	$4.90E^{-9}$	$8.46E^{-9}$	$1.0E^{-9}$	560	2s
S6	2	$3.4021E^{-9}$	$4.1349E^{-9}$	$4.8709E^{-9}$	$2.56E^{-9}$	$9.01E^{-9}$	$1.0E^{-9}$	712	2s
	3	$5.4536E^{-9}$	$5.2303E^{-9}$	$5.1687E^{-9}$	$4.59E^{-9}$	$9.99E^{-9}$	$1.0E^{-9}$	941	2s

Table 5. Numerical, ANN outcomes and error analysis of $\frac{1}{2}\sqrt{Re_r}C_{fx}$ taking $\varphi_{Ag} = 3\%$, $\varphi_{Cu} = 4\%$, $\varphi_{MgO} = 5\%$.

α_1	α_2	ε_T	ε_c	M_a	P_0	Bvp4c approach $\frac{1}{2}\sqrt{Re_r}C_{fx}$	ANN $\frac{1}{2}\sqrt{Re_r}C_{fx}$	Absolute error
0.2	0.2	0.5	0.5	0.2	0.5	2.45352	2.45350	0.00002
0.4	-	-	-	-	-	2.31045	2.31041	0.00004
0.6	-	-	-	-	-	2.32978	2.32969	0.00002
0.2	0.2	0.5	0.5	0.2	0.5	2.32967	2.32966	0.00001
-	0.4	-	-	-	-	2.40034	2.40030	0.00004
-	0.6	-	-	-	-	2.44356	2.44353	0.00003
0.2	0.2	0.5	0.5	0.2	0.5	2.45116	2.45114	0.00002
-	-	0.6	-	-	-	1.51767	1.51766	0.00001
-	-	0.7	-	-	-	1.66785	1.66785	0.00001
0.2	0.2	0.5	0.5	0.2	0.5	2.16890	2.16888	0.00002
-	-	-	0.6	-	-	1.47651	1.47650	0.00001
-	-	-	0.7	-	-	1.46589	1.46587	0.00002
0.2	0.2	0.5	0.5	0.2	0.5	2.44564	2.44563	0.00001
-	-	-	-	0.4	-	2.65895	2.65892	0.00002
-	-	-	-	0.6	-	2.69586	2.69583	0.00003
0.2	0.2	0.5	0.5	0.2	0.5	2.45604	2.45602	0.00002
-	-	-	-	-	0.6	2.25789	2.25786	0.00003
-	-	-	-	-	0.7	2.02342	2.02340	0.00002

every piece of data from the testing, validation, and training stages precisely matches the equality line. There is perfect correlation between the anticipated and actual values, as shown by the training, validation, and testing coefficients of determination values all being exactly 1. The gathered data (R) unequivocally demonstrates that the systems were built to produce precise forecasts. The fitness assessment plots of every scenario in a network model are shown in Figure 8(a–f), together with the errors brought on by variations between the goal and benchmark solutions. The close agreement between target outcomes and reference

Table 6. Numerical, ANN outcomes and error analysis of N_{u_r} taking $\varphi_{Ag} = 3\%$, $\varphi_{Cu} = 4\%$, $\varphi_{MgO} = 5\%$.

α_1	α_2	ε_T	ε_c	M_a	P_0	E_c	Bvp4c approach N_{u_r}	ANN N_{u_r}	Absolute error
0.2	0.2	0.5	0.5	0.2	0.5	0.2	0.35245	0.35242	0.00003
0.4	-	-	-	-	-	-	0.37436	0.37434	0.00002
0.6	-	-	-	-	-	-	0.39416	0.39415	0.00001
0.2	0.2	0.5	0.5	0.2	0.5	0.2	0.37565	0.37564	0.00001
-	0.4	-	-	-	-	-	0.34359	0.34354	0.00005
-	0.6	-	-	-	-	-	0.43056	0.43055	0.00001
0.2	0.2	0.5	0.5	0.2	0.5	0.2	0.45216	0.45214	0.00002
-	-	0.6	-	-	-	-	0.42679	0.47676	0.00003
-	-	0.7	-	-	-	-	0.38055	0. 38053	0.00002
0.2	0.2	0.5	0.5	0.2	0.5	0.2	0.38907	0. 38905	0.00002
-	-	-	0.6	-	-	-	0.40689	0.40688	0.00001
-	-	-	0.7	-	-	-	0.46879	0.46877	0.00002
0.2	0.2	0.5	0.5	0.2	0.5	0.2	0.48987	0.48985	0.00002
-	-	-	-	0.4	-	-	0.49950	0. 49949	0.00001
-	-	-	-	0.6	-	-	0.51586	0.51582	0.00002
0.2	0.2	0.5	0.5	0.2	0.5	0.2	0.45989	0.45987	0.00002
-	-	-	-	-	0.6	-	0.47897	0.47894	0.00003
-	-	-	-	-	0.7	-	0.50234	0.50232	0.00002
0.2	0.2	0.5	0.5	0.2	0.5	0.2	0.46744	0.46742	0.00002
-	-	-	-	-	-	0.3	0.47446	0.47445	0.00001
-	-	-	-	-	-	0.4	0.48086	0.48085	0.00001

Table 7. Numerical, ANN outcomes and error analysis of S_{h_r} taking $\varphi_{Ag} = 3\%$, $\varphi_{Cu} = 4\%$, $\varphi_{MgO} = 5\%$.

α_1	α_2	ε_T	ε_c	M_a	P_0	E_c	Bvp4c approach S_{h_r}	ANN S_{h_r}	Absolute error
0.2	0.2	0.5	0.5	0.2	0.5	0.2	0.12453	0.12452	0.00001
0.4	-	-	-	-	-	-	0.13743	0.13741	0.00002
0.6	-	-	-	-	-	-	0.14165	0.14164	0.00001
0.2	0.2	0.5	0.5	0.2	0.5	0.2	0.13567	0.13566	0.00001
-	0.4	-	-	-	-	-	0.14350	0.14348	0.00002
-	0.6	-	-	-	-	-	0.13962	0.13961	0.00001
0.2	0.2	0.5	0.5	0.2	0.5	0.2	0.14212	0.14210	0.00002
-	-	0.6	-	-	-	-	0.16794	0.16793	0.00001
-	-	0.7	-	-	-	-	0.18059	0.18058	0.00001
0.2	0.2	0.5	0.5	0.2	0.5	0.2	0.13890	0.13889	0.00001
-	-	-	0.6	-	-	-	0.14680	0.14678	0.00002
-	-	-	0.7	-	-	-	0.15687	0.15685	0.00002
0.2	0.2	0.5	0.5	0.2	0.5	0.2	0.13898	0.13897	0.00001
-	-	-	-	0.4	-	-	0.12950	0.12949	0.00001
-	-	-	-	0.6	-	-	0.11580	0.11578	0.00002
0.2	0.2	0.5	0.5	0.2	0.5	0.2	0.14920	0.14919	0.00001
-	-	-	-	-	0.6	-	0.15782	0.15781	0.00001
-	-	-	-	-	0.7	-	0.16230	0.16229	0.00001
0.2	0.2	0.5	0.5	0.2	0.5	0.2	0.14674	0.14673	0.00001
-	-	-	-	-	-	0.3	0.17786	0.17784	0.00001
-	-	-	-	-	-	0.4	0.20845	0.20844	0.00001

profiles across all models validates the precision of the neural network framework.

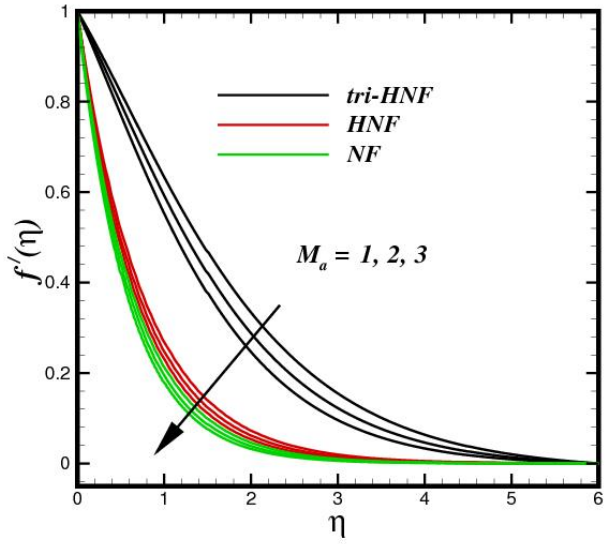

Figure 9. Flow performance of various fluid by uplifting M_a.

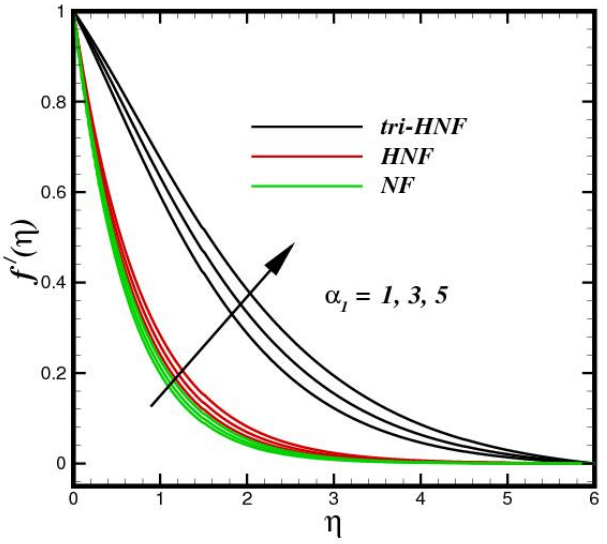

Figure 11. Flow performance of various fluid by uplifting α_1.

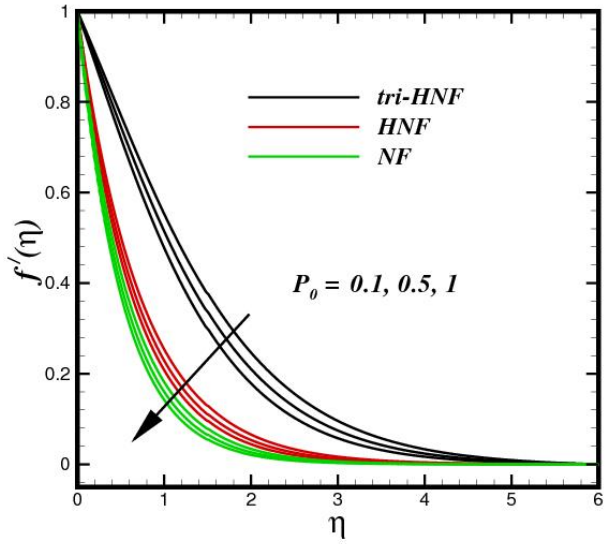

Figure 10. Flow performance of various fluid by uplifting P_0.

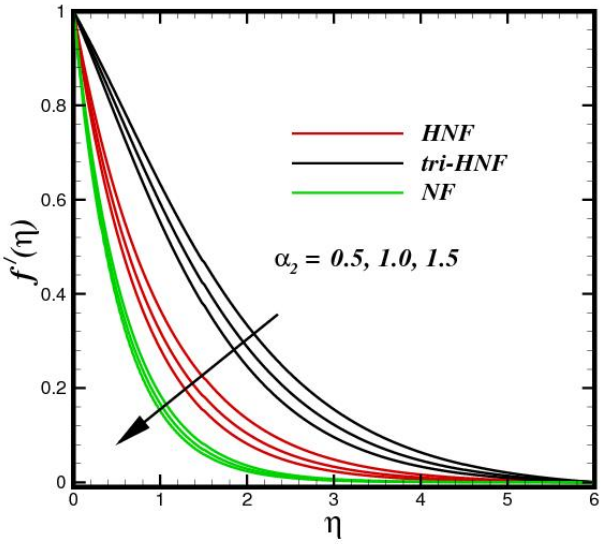

Figure 12. Flow performance of various fluid by uplifting α_2.

Figure 9, shows the impact of the magnetic parameter M_a on the velocity profile $f'(\eta)$. Each plot includes comparison of Boger tri-HNF, HNF, and mono-NF. The BLF is restricted by higher estimation of M_a. Physically, the Lorentz force, which is generated by the magnetic range opposes the fluid movement. Figure 10, illustrates the impact of the porosity parameter P_0 on $f'(\eta)$. Momentum decreases when the porosity parameter increases because increased permeability promotes fluid flow in porous medium faster by lowering impedance. The Darcy's law, which governs fluid flow in permeable media, states that these two-layered variations for HNF, NF, and tri-HNF result in lesser momentum transfer as the fluid encounters less obstruction. The velocity performance for an increase in solvent parameter α_1 is displayed in Figure 11. It is demonstrated that the velocity distribution is enhanced by raising the solvent fraction parameter α_1. Phyiscally, the Boger tri-HNF is extremely elastic due to its greater flow rate at low Reynolds number $Re_r < 100$ and constant viscosity. High α_2 increases viscosity within the boundaries,

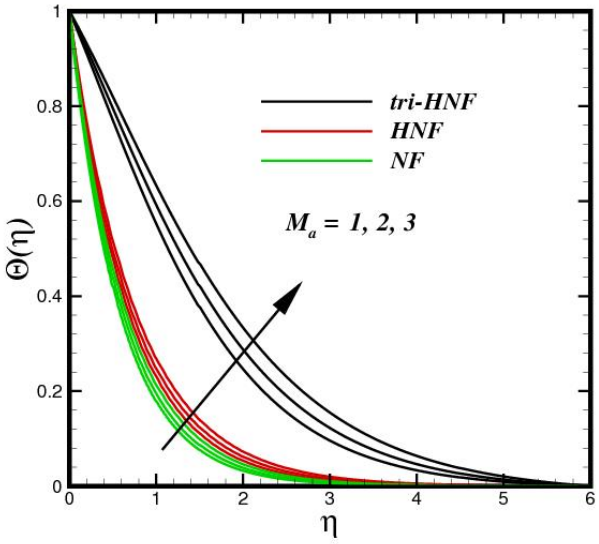

Figure 13. Thermal performance of various fluid by uplifting M_a.

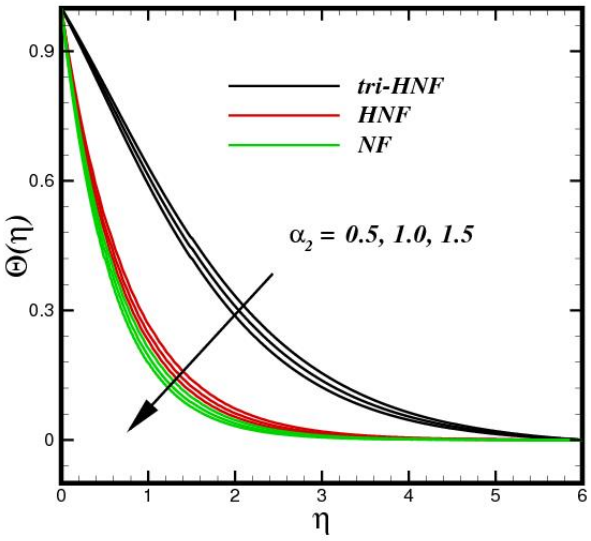

Figure 15. Thermal performance of various fluid by uplifting α_2.

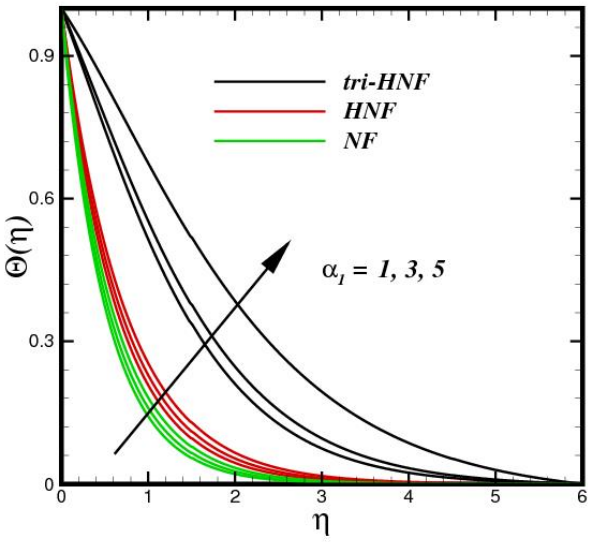

Figure 14. Thermal performance of various fluid by uplifting α_1.

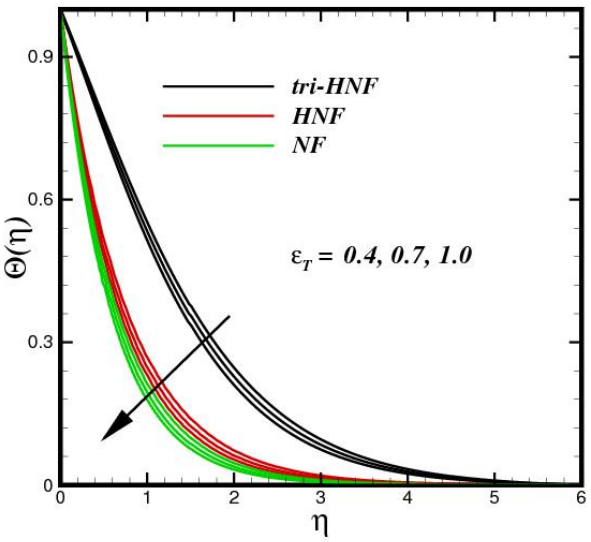

Figure 16. Thermal performance of various fluid by uplifting ε_T.

which lowers velocity, as shown in Figure 12. In all three types of fluids, it is found that the fluid flow behaviors decline gradually as the relaxation time ratio α_2 values rise. But for both momentum BL thicknesses, the boost is much more noticeable in tri-HNF, which is explained by the Boger tri-HNF intrinsically high elasticity. The balance between viscosity and elasticity in a non-Newtonian fluid is characterized physically by α_2.

The effect of M_a on the temperature distribution $\Theta(\eta)$ is examined in Figure 13. Phyiscally, when a magnetic field is applied, a Lorentz force is created. This resistive force works against fluid motion. This resistance raises the temperature distribution by converting kinetic energy into heat energy. Collectively, these findings highlight how this parameters interact to regulate temperature behaviour and heat transport in the fluid system. The rise in temperature is significant in tri-HNF $\varphi_{Ag} = 3\%$, $\varphi_{Cu} = 4\%$, $\varphi_{MgO} = 5\%$, because of increase thermal conductivity of nanomaterial of base fluid. The response of solvent fraction factor α_1 on temperature profile $\Theta(\eta)$ is shown in Figure 14.

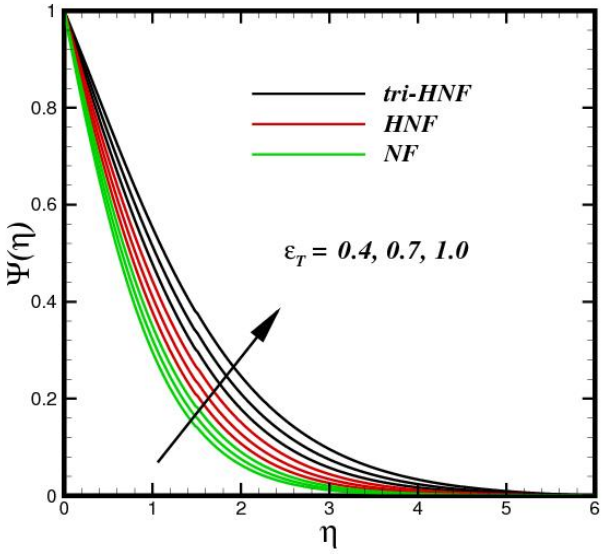

Figure 17. Concentration performance of various fluid by uplifting ε_T.

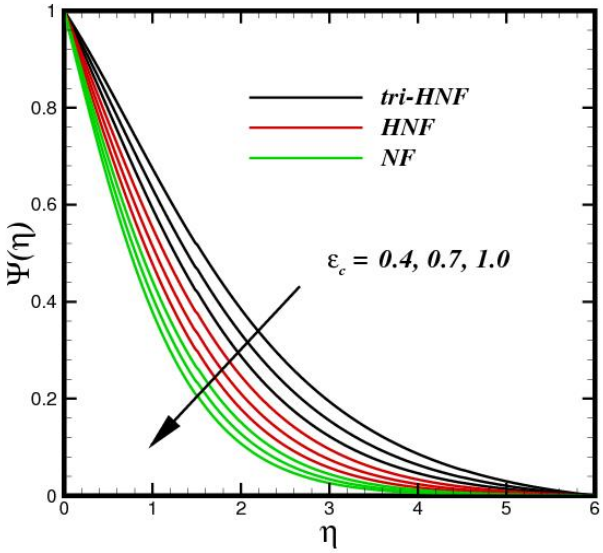

Figure 18. Concentration performance of various fluid by uplifting ε_c.

It demonstrates how the temperature rises with an increase in α_1 input. Physically, the Boger fluid strong elasticity at constant viscosity and small Reynolds number increase the velocity rate. Consequently, as the solvent fraction strength increases, the thermal boundary rises, raising the electrically charged particles. As seen in Figure 15, the temperature drops, when α_2 is increased. The dispersion of heat decreases at the disk surface. The Cattaneo-Christov heat flux model thermal relaxation parameter ε_T accounts for finite thermal diffusion speed by introducing a temporal delay among the temperature difference and heat flux. Improvements in this parameter ε_T slow down heat transfer, which reduces thermal diffusion and temperature buildup close to the stretched disk as shown in Figure 16. The physical manifestation of this is a change from immediate Fourier-type conduction to non-equilibrium heat transfer, in which the fluid holds onto thermal energy for a longer period of time, raising local temperature profiles and postponing thermal equilibrium in the BL.

The influece of thermal and soluatal relaxation parameter on concetration is depicted in Figure 17 and Figure 18. In lag time among a concentration gradient and the subsequent mass diffusion is taken into account by the solutal relaxation parameter. The slower mass transit caused by a rise in this parameter modifies the concentration BL and indirectly influences temperature through coupled thermo-solutal interactions. Localized accumulation of heat may result from a greater solutal relaxation value because species diffusion affects thermal transport. The Boger tri-HNF and other viscoelastic fluids exhibit non-Fickian mass transfer and thermal coupling. These variables work together to produce a more robust and constrained solute boundary layer, where thermally induced species transfer and slower mass diffusion raise local concentrations while postponing equilibrium.

6 Conclusion

The present study investigates the impact of the Cattaneo-Christov heat and mass fluxes model on the Boger tri-HNF under magnetic field conditions. The fluid flow across a stretching disk follows the Oberbeck-Boussinesq approximation. The dynamics of the flow are influenced by Lorentz forces, disk porosity, slip effects, and viscous dissipation. The Bvp4c method was used to solve the nonlinear PDE that described the governing flow. The accuracy of the numerical solutions was predicted and confirmed using the LM-ANN model. The model integrates novel machine learning mechanism for Boger tri-HNF under the impact of Cattaneo-Christov heat and mass fluxes model. With an average error of 10^{-9}, the ANN model performs exceptionally well in training, testing, and validation for the current project. The accuracy and consistency of the LM-ANN prediction outputs and numerical solutions are demonstrated by achieving a degree of perfection between 10^{-10} and 10^{-4}. Results are validated using information gleaned from numerical tables, efficiency, regression, velocity,

temperature, concentration, and error histogram graphical representations. The following summarizes the key conclusions of the study:

- Velocity and temperature of tri-HNF uplift with solvent parameter $\alpha 1$, while an opposite trend was seen against magnetic parameter M_a. Similar trend for flow and temperature was achieved for the relaxation time ratio $\alpha 2$.
- Impact of M_a on velocity and temperature was contradictory.
- The thermal and solutal relaxation parameter depict similar trend on temperature and concentration, respectively.
- The ratio parameter, thermal relaxation parameter, and solutal relaxation parameter show a declining trend, whereas the rate of heat and mass transfer increases with increasing values of the magnetic, solvent viscosity, and slip parameters.
- Augmentations in solvent viscosity and slip decline the wall stresses.
- Measurements indicate that the absolute error for skin friction, Nusselt, and Sherwood numbers compared to the actual values and the ANN predicted values falls between 10^{-4} to 10^{-5}.
- The study central hypothesis is directly validated by the effective use and validation of the ANN framework, as shown by the low MSE and strong correlation index. The results demonstrate that the AI framework is a reliable and accurate method for examining the intricate relationships among three distinct nanoparticles, the Boger fluid, MHD effects, and the CCHF over a porous disk.

Limitation of this research: The ANN and a numerical framework was trained on a produced dataset, rather than experimental data, serve as the study main limitations. Although the model was verified against earlier research in a restricted setting, it ignores the intricacies and possible variations that would be present in an actual physical experiment. Therefore, the study result is very dependent on how accurately it uses computing and might not fully account for all the complexities of the physical system.

Future studies: The present study can be extended in the future by using experimental data to validate its theoretical model and AI framework. Complex physical phenomena such as Hall currents, Joule heating, or various features of porous media can also be included in future studies. The practical utility of the current framework would also be expanded by applying it to different geometries, like pipelines or channels, and by utilizing more sophisticated AI algorithms. A thorough examination of entropy creation may also shed light on the system's thermodynamic efficiency.

Data Availability Statement

Data will be made available on request.

Funding

This work was supported without any funding.

Conflicts of Interest

The author declares no conflicts of interest.

Ethical Approval and Consent to Participate

Not applicable.

References

[1] James, D. F. (2009). Boger fluids. *Annual Review of Fluid Mechanics, 41*(1), 129-142. [Crossref]

[2] Jebali, M., Rehman, S., Bouzidi, M., Shamshad, M., & Nasr, S. (2025). Optimization of magneto-thin film bioconvection flow of bi-viscosity Bingham fluid with swarm microorganism using machine learning-integrated numerical simulations. *Physics of Fluids, 37*(9). [Crossref]

[3] Jackson, K. P., Walters, K., & Williams, R. W. (1984). A rheometrical study of boger fluids. *Journal of Non-Newtonian Fluid Mechanics, 14*, 173-188. [Crossref]

[4] Nasr, S., Rehman, S., Znaidia, S., & Ahmed, W. (2025). Boundary layer flow and heat-mass transfer of shear-thinning nanofluid past a thin needle: Electroperiodic magnetic field and thermo-diffusion effects. *Nuclear Engineering and Technology, 57*(5), 103354. [Crossref]

[5] James, D. F., & Roos, C. A. (2021). Pressure drop of a Boger fluid in a converging channel. *Journal of Non-Newtonian Fluid Mechanics, 293*, 104557. [Crossref]

[6] López-Aguilar, J. E., Tamaddon-Jahromi, H. R., Webster, M. F., & Walters, K. (2016). Numerical vs experimental pressure drops for Boger fluids in sharp-corner contraction flow. *Physics of Fluids, 28*(10). [Crossref]

[7] Choujaa, M. H., Riahi, M., & Aniss, S. (2025). Inertio-elastic parametric resonance between

inertia-dominated and elasticity-dominated Taylor vortex flows in Boger fluids confined between two co-oscillating cylinders. *Journal of Non-Newtonian Fluid Mechanics, 338*, 105398. [Crossref]

[8] Raza, Q., Wang, X., Mushtaq, T., Ali, B., & Shah, N. A. (2025). Finite element analysis of nanolayer thermal conductivity in Boger nanofluid flow with radius of nanoparticle and motile microorganisms under time-dependent conditions. *Chaos, Solitons & Fractals, 194*, 116205. [Crossref]

[9] Raza, Q., Wang, X., & Ali, B. (2025). Influence of viscosity and thermal conductivity in Boger nanofluid flow through porous disk: finite difference analysis. *Journal of Thermal Analysis and Calorimetry, 150*(1), 451-477. [Crossref]

[10] Ali, B., Sharif, H., Habib, D., Ghazwani, H. A., Saman, I., & Yang, H. (2024). Significance of tri-hybrid nanoparticles in thermal management subject to magnetized squeezing flow of a Boger-micropolar nanofluid between concentring disks. *Journal of Molecular Liquids, 397*, 124141. [Crossref]

[11] Sheykhian, M. K., Kayhani, M. H., Norouzi, M., Kim, M., & Kim, K. C. (2023). An experimental study on the impact of Boger and Newtonian droplets on spherical surfaces. *Physics of Fluids, 35*(8). [Crossref]

[12] Labbé, R., Pinton, J. F., & Fauve, S. (1996). Study of the von Kármán flow between coaxial corotating disks. *Physics of Fluids, 8*(4), 914-922. [Crossref]

[13] Zandbergen, P. J., & Dijkstra, D. (1987). Von Kármán swirling flows. *Annual review of fluid mechanics, 19*, 465-491. [Crossref]

[14] Turkyilmazoglu, M. (2015). Bödewadt flow and heat transfer over a stretching stationary disk. *International Journal of Mechanical Sciences, 90*, 246-250. [Crossref]

[15] Chu, Y. M., Al-Khaled, K., Khan, N., Khan, M. I., Khan, S. U., Hashmi, M. S., ... & Tlili, I. (2021). Study of Buongiorno's nanofluid model for flow due to stretching disks in presence of gyrotactic microorganisms. *Ain Shams Engineering Journal, 12*(4), 3975-3985. [Crossref]

[16] Khan, U., Bilal, S., Zaib, A., Makinde, O. D., & Wakif, A. (2022). Numerical simulation of a nonlinear coupled differential system describing a convective flow of Casson gold–blood nanofluid through a stretched rotating rigid disk in the presence of Lorentz forces and nonlinear thermal radiation. *Numerical Methods for Partial Differential Equations, 38*(3), 308-328. [Crossref]

[17] Sharma, K., Vijay, N., Mabood, F., & Badruddin, I. A. (2022). Numerical simulation of heat and mass transfer in magnetic nanofluid flow by a rotating disk with variable fluid properties. *International Communications in Heat and Mass Transfer, 133*, 105977. [Crossref]

[18] Rehman, S. (2025). Boundary layer slip flow and heat-mass transfer of radiated water based nanofluid over a permeable disk: Darcy-Forchheimer model and activation energy. *Chaos, Solitons & Fractals, 192*, 116097. [Crossref]

[19] Khan, M. I., & Alzahrani, F. (2020). Transportation of heat through Cattaneo-Christov heat flux model in non-Newtonian fluid subject to internal resistance of particles. *Applied Mathematics and Mechanics, 41*(8), 1157-1166. [Crossref]

[20] Fourier, J. B. J. (1888). *Théorie analytique de la chaleur*. Gauthier-Villars et fils. [Crossref]

[21] Cattaneo, C. (1948). Sulla conduzione del calore. *Atti Sem. Mat. Fis. Univ. Modena, 3*, 83-101. [Crossref]

[22] Christov, C. I. (2009). On frame indifferent formulation of the Maxwell–Cattaneo model of finite-speed heat conduction. *Mechanics research communications, 36*(4), 481-486. [Crossref]

[23] MN, P., SK, N., & Vajravelu, K. (2025). Heat and mass transfer in Casson fluid flow with tri-hybrid nanoparticles on curved surface: A biomedical relevance. *Physics of Fluids, 37*(8). [Crossref]

[24] Deb, P., & Layek, G. C. (2025). Multistability and transition to chaos in non-Fourier convection under cross-flow forcing. *Physics of Fluids, 37*(9). [Crossref]

[25] Saravanan, S., & Muthumeena, R. (2025). Onset of thermal turbulence in Cattaneo-type convection inside a heater mounted enclosure. *Physics of Fluids, 37*(7). [Crossref]

[26] Jia, B., & Jian, Y. (2025). Role of the Maxwell–Cattaneo effect on convection instability in a vertical Brinkman porous layer. *Physics of Fluids, 37*(4). [Crossref]

[27] Shah, F., Zhang, D., & Linlin, G. (2024). Non-similar analysis of two-phase hybrid nano-fluid flow with Cattaneo-Christov heat flux model: a computational study. *Engineering Applications of Computational Fluid Mechanics, 18*(1), 2380800. [Crossref]

[28] Choi, S. U. (1995, November). Enhancing thermal conductivity of fluids with nanoparticles. In *ASME international mechanical engineering congress and exposition* (Vol. 17421, pp. 99-105). American Society of Mechanical Engineers. [Crossref]

[29] Khan, S. A., Razzaq, A., Hayat, T., & Razaq, A. (2025). Artificial neural network analysis for entropy optimized flow of Jeffrey nanofluid invoking Cattaneo-Christov theory. *Energy*, 137998. [Crossref]

[30] Afridi, M. I., Almohsen, B., Habib, S., Khan, Z., & Razzaq, R. (2025). Artificial neural network analysis of MHD Maxwell nanofluid flow over a porous medium in presence of Joule heating and nonlinear radiation effects. *Chaos, Solitons & Fractals, 192*, 116072. [Crossref]

[31] Yasmin, H., Bossly, R., Alduais, F. S., Al-Bossly, A., & Saeed, A. (2025). Thermally radiative water-based hybrid nanofluid with nanoparticles and gyrotactic microorganisms past a stretching surface with convective conditions and porous media. *Case Studies in Thermal Engineering, 65*, 105644. [Crossref]

[32] Adogbeji, V. O., Atofarati, E. O., Govinder, K., Sharifpur, M., & Meyer, J. P. (2025). Tri-hybrid nanofluids for thermal applications: stability, magneto-hydrodynamics, and machine learning prediction. *Multiscale and Multidisciplinary Modeling, Experiments and Design, 8*(9), 411. [Crossref]

[33] Anjum, M. W., Saqib, S. U., Shih, Y. T., Jaghdam, I. H., Becheikh, N., & Kolsi, L. (2025). An Intelligent Soft Computing Model for Predicting the Thermal Behavior of Blood-Based Trihybrid Nanofluids Flow in Biomedical Drug Delivery Applications. *Case Studies in Thermal Engineering*, 106742. [Crossref]

[34] Rauf, A., Faisal, Hussain, F., & Shah, N. A. (2025). A numerical study of Carreau–Yasuda tri-hybrid nanofluid over a convective heated surface near a stagnation point. *Journal of Thermal Analysis and Calorimetry*, 1-12. [Crossref]

[35] Algehyne, E. A., Alrihieli, H. F., Bilal, M., Saeed, A., & Weera, W. (2022). Numerical approach toward ternary hybrid nanofluid flow using variable diffusion and non-Fourier's concept. *ACS omega, 7*(33), 29380-29390. [Crossref]

[36] Shah, T. R., Koten, H., & Ali, H. M. (2020). Performance effecting parameters of hybrid nanofluids. In *Hybrid nanofluids for convection heat transfer* (pp. 179-213). Academic Press. [Crossref]

[37] Anwar, T., Kumam, P., Almutairi, K. S., & Watthayu, W. (2025). Thermophysical dynamics of mineral oil-based hybrid nanofluids under multiple flow conditions and radiation effects; Individual, synergistic, and shape impacts analysis. *Journal of Radiation Research and Applied Sciences, 18*(4), 101748. [Crossref]

[38] Ragulkumar, E., & Anwar, T. (2025). Heat and mass transfer of a 2D monolayer hybrid nanofluid over a vertical cone subject to magnetic, porosity, and chemical reaction impacts. *International Journal of Thermofluids*, 101387. [Crossref]

[39] Rafique, K., Mahmood, Z., Popa, I. L., Anwar, T., & Kumar, A. (2025). Double diffusive convection in non-newtonian fluid flow with quadratic radiation and variable viscosity: Heat generation effects in lower stagnation point of solid sphere. *Results in Engineering, 27*, 106820. [Crossref]

[40] Mukherjee, I., & Routroy, S. (2012). Comparing the performance of neural networks developed by using Levenberg–Marquardt and Quasi-Newton with the gradient descent algorithm for modelling a multiple response grinding process. *Expert Systems with Applications, 39*(3), 2397-2407. [Crossref]

[41] Aljohani, J. L., Alaidarous, E. S., Raja, M. A. Z., Shoaib, M., & Alhothuali, M. S. (2021). Intelligent computing through neural networks for numerical treatment of non-Newtonian wire coating analysis model. *Scientific Reports, 11*(1), 9072. [Crossref]

[42] Raja, M. A. Z., Mehmood, A., ur Rehman, A., Khan, A., & Zameer, A. (2018). Bio-inspired computational heuristics for Sisko fluid flow and heat transfer models. *Applied Soft Computing, 71*, 622-648. [Crossref]

[43] Housiadas, K. D., & Tsangaris, C. (2023). Channel flow with variable geometry and Navier slip at the walls using high-order lubrication theory. *European Journal of Mechanics-B/Fluids, 98*, 194-207. [Crossref]

[44] Khan, W. A., Khan, M., Alshomrani, A. S., & Ahmad, L. (2016). Numerical investigation of generalized Fourier's and Fick's laws for Sisko fluid flow. *Journal of Molecular Liquids, 224*, 1016-1021. [Crossref]

[45] Sousa, P. C., Coelho, P. M., Oliveira, M. S. N., & Alves, M. A. (2009). Three-dimensional flow of Newtonian and Boger fluids in square–square contractions. *Journal of non-newtonian fluid mechanics, 160*(2-3), 122-139. [Crossref]

[46] Abbas, M., Khan, N., Hashmi, M. S., Tawfiq, F. M., Inc, M., & Raghunatha, K. R. (2024). Numerical simulation of chemical reactive flow of Boger fluid over a sheet with heat source and local thermal non-equilibrium conditions. *Case Studies in Thermal Engineering, 59*, 104498. [Crossref]

[47] Madkhali, H. A., Haneef, M., El-Shafay, A. S., Alharbi, S. O., & Nawaz, M. (2022). Mixed convective transport in Maxwell hybrid nano-fluid under generalized Fourier and Fick laws. *International Communications in Heat and Mass Transfer, 130*, 105714. [Crossref]

[48] Waqas, M., Naz, S., Hayat, T., Shehzad, S. A., & Alsaedi, A. (2019). Effectiveness of improved Fourier-Fick laws in a stratified non-Newtonian fluid with variable fluid characteristics. *International Journal of Numerical Methods for Heat & Fluid Flow, 29*(6), 2128-2145. [Crossref]

[49] Muzammal, M., Farooq, M., Moussa, S. B., & NASR, S. (2024). Melting heat transfer of a quadratic stratified Jeffrey nanofluid flow with inclined magnetic field and thermophoresis. *Alexandria Engineering Journal, 103*, 158-168. [Crossref]

[50] Madhu, J., Vinutha, K., Kumar, R. N., Gowda, R. P., Prasannakumara, B. C., Alqahtani, A. S., & Malik, M. Y. (2024). Impact of solid-liquid interfacial layer in the nanofluid flow between stretching stationary disk and a rotating cone. *Tribology International, 192*, 109187. [Crossref]

[51] Rafique, K., Mahmood, Z., Khan, U., Eldin, S. M., Oreijah, M., Guedri, K., & Khalifa, H. A. E. W. (2023). Investigation of thermal stratification with velocity slip and variable viscosity on MHD flow of Al2O3-Cu- TiO2/H2O nanofluid over disk. *Case Studies in Thermal Engineering, 49*, 103292. [Crossref]

[52] Rauf, A., Shehzad, S. A., Kiran, R., Mustafa, F., Ali, I., Khan, S., & Siddiq, M. K. (2024). Regression and numerical treatment of micropolar fluid induced by the melting stretchable disk. *Case Studies in Thermal Engineering, 56*, 104236. [Crossref]

[53] Turkyilmazoglu, M. (2012). Three dimensional MHD stagnation flow due to a stretchable rotating disk.

International Journal of Heat and Mass Transfer, 55(23-24), 6959-6965. [Crossref]

[54] Khlifi, M. A., Mahroogi, F., & Tlili, I. (2025). Thermal Insight to Magnetized Tri Hybrid Nanofluid (CuO-TiO2-SiO2)/blood with Nonlinear Radiated Effects: Applications to Hyperthermia Cancer Treatment. *Case Studies in Thermal Engineering*, 106235. [Crossref]

[55] Abu Bakar, S., Wahid, N. S., Md Arifin, N., & Pop, I. (2025). Optimization of heat transfer on Jeffrey ternary nanofluid flow with slip conditions and heat generation by response surface methodology. *Multiscale and Multidisciplinary Modeling, Experiments and Design, 8*(2), 150. [Crossref]

[56] Abbas, M., Khan, N., Hashmi, M. S., Salleh, Z., Aly, A. A., Rezapour, S., & Inc, M. (2024). Consequence of Cattaneo-Christov heat and mass flux models on bioconvective flow of dusty hybrid nanofluid over a Riga plate in the presence of gyrotactic microorganisms and Stephan blowing impacts. *Case Studies in Thermal Engineering, 61*, 105061. [Crossref]

[57] Mahmood, Z., Eldin, S. M., Rafique, K., & Khan, U. (2023). Numerical analysis of MHD tri-hybrid nanofluid over a nonlinear stretching/shrinking sheet with heat generation/absorption and slip conditions. *Alexandria Engineering Journal, 76*, 799-819. [Crossref]

[58] Ali, B., Jubair, S., Aluraikan, A., Abd El-Rahman, M., Eldin, S. M., & Khalifa, H. A. E. W. (2023). Numerical investigation of heat source induced thermal slip effect on trihybrid nanofluid flow over a stretching surface. *Results in Engineering, 20*, 101536. [Crossref]

[59] Khashi'ie, N. S., Arifin, N. M., & Pop, I. (2021). Unsteady axisymmetric flow and heat transfer of a hybrid nanofluid over a permeable stretching/shrinking disc. *International Journal of Numerical Methods for Heat & Fluid Flow, 31*(6), 2005-2021. [Crossref]

[60] Rafique, K., Mahmood, Z., Adnan, Muhammad, T., Alqahtani, H., & Shaaban, A. A. (2025). Dynamics of shape factor with Joule heating and thermal stratification on magnetohydrodynamic A l 2 O 3-C u-T i O 2/H 2 O nanofluid of stretching disk: an irreversibility analysis. *Journal of Thermal Analysis and Calorimetry, 150*(4), 2757-2780. [Crossref]

[61] Azhar, E., Maraj, E. N., Afaq, H., Jamal, M., & Iqbal, Z. (2024). Application of activation energy and Joule heating with variable viscosity on MHD flow of trihybrid nanofluid over a disk. *International Communications in Heat and Mass Transfer, 155*, 107573. [Crossref]

[62] Iqbal, J., Abbasi, F. M., & Ali, I. (2024). Heat transfer analysis for magnetohydrodynamic peristalsis of Reiner–Philippoff fluid: Application of an artificial neural network. *Physics of Fluids, 36*(4). [Crossref]

[63] Shafiq, A., Çolak, A. B., & Sindhu, T. N. (2023). Modeling of Soret and Dufour's convective heat transfer in nanofluid flow through a moving needle with artificial neural network. *Arabian Journal for Science and Engineering, 48*(3), 2807-2820. [Crossref]

[64] Agatonovic-Kustrin, S., & Beresford, R. (2000). Basic concepts of artificial neural network (ANN) modeling and its application in pharmaceutical research. *Journal of pharmaceutical and biomedical analysis, 22*(5), 717-727. [Crossref]